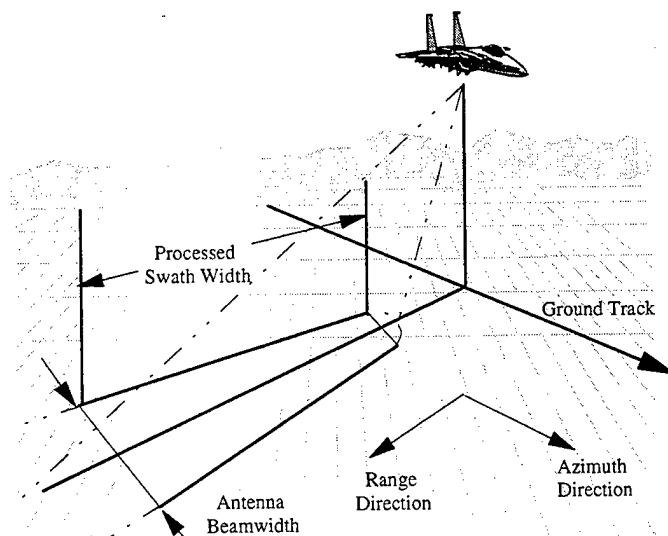WL-TR-97-1185

INTEGRATED SYNTHETIC APERTURE RADAR AND NAVIGATION SYSTEMS FOR TARGETING APPLICATIONS

Jeffery R. Layne, Ph.D. and Lt Erik P. Blasch
Fusion Technology Branch
Combat Information Division
Avionics Directorate

September 1997

FINAL REPORT FOR PERIOD 12/01/92 - 12/01/93

Approved for public release; distribution unlimited

19980210 112

AVIONICS DIRECTORATE
WRIGHT LABORATORY   DTIC QUALITY INSPECTED 3
AIR FORCE MATERIEL COMMAND
WRIGHT-PATTERSON AIR FORCE BASE, OH 45433-7623

NOTICE

This technical report has been reviewed and is approved for publication.

Jeffery R. Layne, Ph.D.
Electronics Engineer

William R. Baker, Chief
Fusion Technology Branch

FOR THE COMMANDER

Jerry L. Covert, Chief
Combat Information Division
Avionics Directorate

REPORT DOCUMENTATION PAGE		*Form Approved* *OMB No. 0704-0188*

1. AGENCY USE ONLY *(Leave blank)*	2. REPORT DATE September 1997	3. REPORT TYPE AND DATES COVERED Final 12/01/92 -12/01/93

4. TITLE AND SUBTITLE
Integrated Synthetic Aperture Radar and Navigation Systems for Targeting Applications

5. FUNDING NUMBERS

6. AUTHOR(S)
Jeffery R. Layne, Ph.D. and
Lt. Erik Blasch

7. PERFORMING ORGANIZATION NAME(S) AND ADDRESS(ES)
WL/AACF
2241 Avionics Circle
WPAFB, Ohio 45433-7318

8. PERFORMING ORGANIZATION REPORT NUMBER

9. SPONSORING/MONITORING AGENCY NAME(S) AND ADDRESS(ES)
Jeffery R. Layne, WL/AACF (937)255-1491 ext. 3325
Avionics Directorate
Wright Laboratory
Air Force Materiel Command
Wright-Patterson AFB OH 45433-7623

10. SPONSORING/MONITORING AGENCY REPORT NUMBER

WL-TR-97-1185

11. SUPPLEMENTARY NOTES

12a. DISTRIBUTION AVAILABILITY STATEMENT
Approved for public release, distribution unlimited

12b. DISTRIBUTION CODE

13. ABSTRACT *(Maximum 200 words)*

High resolution image data produced by a SAR is often employed with a monopulse radar to locate fixed ground based target. However, as with any measuring device, there exists some "uncertainty" or "error" in target location. By combining the SAR measurements and monopulse radar measurements with measurements from other sensors, we hope to reduce the level of uncertainty in target location. The goal here is to bring together information from SAR and navigation sensors such as global positioning system (GPS) receiver and/or an inertial navigation system (INS). This report focuses on the integration of measurements from a SAR and an INS in a Kalman filter. Many of the points developed here have been presented in other documents. However, the intent of this document is to bring together some of these ideas to implement SAR measurements in a centralized Kalman filter. The goal is to enhance the overall system accuracy.

14. SUBJECT TERMS

Synthetic Aperature Radar	Kalman Filter	
Navigation	Integration	
Targeting		

15. NUMBER OF PAGES
53

16. PRICE CODE

17. SECURITY CLASSIFICATION OF REPORT	18. SECURITY CLASSIFICATION OF THIS PAGE	19. SECURITY CLASSIFICATION OF ABSTRACT	20. LIMITATION OF ABSTRACT
Unclassified	Unclassified	Unclassified	UL

TABLE OF CONTENTS

LIST OF FIGURES

LIST OF TABLES

1.0 Introduction

Synthetic Aperture Radar (SAR) is an airborne radar capable of generating high resolution images of surface target areas and terrain. The term *Synthetic Aperture* is used because the radar utilizes the motion of the aircraft, or other platform, to synthesize the effect of a large aperture antenna from a physically small aperture antenna. As a result, high resolution images can be obtained from a SAR using an antenna which would otherwise produce poor resolution.

The high resolution image data produced by a SAR is often employed with a monopulse radar to locate fixed ground based target. However, as with any measuring device, there exists some "uncertainty" or "error" in target location. By combining the SAR measurements and monopulse radar measurements with measurements from other sensors, we hope to reduce the level of uncertainty in target location. The goal here is to bring together information from SAR and navigation sensors such as global positioning system (GPS) receiver and/or an inertial navigation system (INS). This report focuses on the integration of measurements from a SAR and an INS in a Kalman filter.

The contents of this report may be summarized as follows:
   1) describe the operation of a SAR
   2) describe the operation of monopulse radar,
   3) describe how a target's location is computed from SAR and monopulse radar measurements,
   4) present error models for both SAR and monopulse radar measurements,
   5) derive the Kalman filter measurement error models

Many of the points developed here have been presented in other documents [1, 2, 3, 4, 5, 6, 7, 8]. The intent of this document is to bring together some of these ideas to implement SAR Measurements in a centralized Kalman filter. The goal is to enhance the overall system accuracy.

A thorough understanding of how SAR measurements are obtained is needed to employ SAR measurements in a Kalman filter. Therefore, the first few sections of this report provide the basic background and develop models for SAR measurements. In Section 2, a brief overview of SAR processing techniques is presented. This overview includes a description of unfocused line-by-line processing, focused line-by-line, and Doppler processing. Highlighted in this discussion are the measurements that are inherently available from a SAR for computing a target's location. Also, explained are the differences between stripmap mode and spotlight mode SAR. Section 3 includes a brief discussion on monopulse radar. Section 4 provides an introduction to the geometry of SAR and monopulse radar measurements. Presented here are the coordinate frames and coordinate frame transformation used throughout this report. Also, presented in this section are some basic mathematical relationships needed in

later sections on measurement models. Presented in Section 5 is a method for computing a target's location from SAR measurements and monopulse radar measurements. Section 6 presents a truth model for both the SAR range and range rate measurements and the monopulse radar azimuth and elevation measurements. This section includes a detailed stochastic model for all errors present in radar measurements.

To generate a measurement for a Kalman filter, the INS outputs must be related geometrically to the SAR and monopulse radar measurements. Section 7 describes how to compute, from INS indicated outputs, quantities that are similar to each radar measurement. These computed quantities are referenced in this report as the INS *indicated measurements*. In essence, this section describes the geometric relationships between INS outputs and radar measurements. Section 8, derives the linearized INS indicated measurements. This includes a perturbation analysis which describes the sensitivity of the INS output errors on the computed INS indicated measurements. The linearized measurement equations derived in Section 8 are used in Section 9 to derive the linearized measurement equations needed in a Kalman filter.

Finally, the last few sections provide a summary of the radar and INS error models. Section 10 summarizes the dynamic equations for the INS and radar error states. Section 11 summarizes the measurement equations needed to implement a Kalman filter. Section 12 summarizes a typical error budget for a SAR/INS integration. Section 13 provides some final remarks on many of the points derived in this report.

2.0 Synthetic Aperture Radar Background

The primary function of a SAR is to generate high resolution radar images of ground terrain. These SAR images are often clear enough for an operator to recognize man-made targets on the ground. As a result, SAR images are employed to achieve the first task in targeting, namely target designation. The operator designates the target manually placing a cursor over the desired target in the image. Once the target is designated, SAR systems often employ conventional radar techniques to actually locate the target. For instance, the range (r) and range rate ($\dot{r}$) to a given target can be computed by the following equations:

$$r = \frac{cT}{2} \tag{1}$$

$$\dot{r} = \frac{cF_d}{2F} \tag{2}$$

where c is the speed of light, T is the round-trip transit time of the transmitted radar pulse, F_d is the Doppler frequency shift, and F is the frequency of the transmitted signal.

The basic SAR geometry is shown in Figure 1. The SAR is characterized by a wide beam antenna which illuminates a large area on the ground. For what is assumed an instant in time, the SAR transmits a radar pulse and samples the magnitude and phase of the return signal. Since radar waves propagate at nearly a constant speed in the Earth's atmosphere, the earliest samples correspond to the points on the ground nearest the aircraft. Likewise, the return from more distant points are represented by later samples. The samples are stored in vectors of data referred to **as *range bins***. Figure 1 illustrates the area on the ground for which magnitude and phase information are collected by the SAR for a given transmitted pulse.
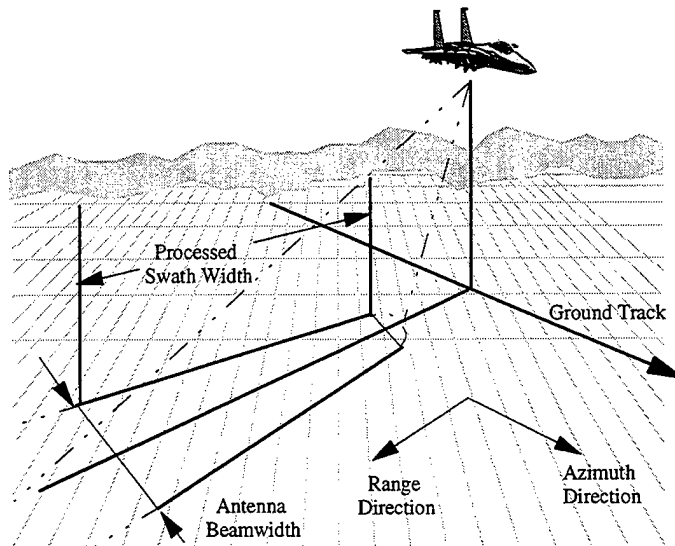
Figure 1. SAR Geometry.

As the aircraft travels along a given ground track, the process of illuminating the ground with a radar signal and sampling the magnitude and phase of the return is repeated every T seconds for consecutively overlapping areas on the ground. As shown in Figure 2, the result is a two dimensional array of data which contains magnitude and phase information of the radar returns in both range and azimuth directions.

It is possible to generate a radar image directly from the two dimensional array of magnitude and phase data. However, due to the use of a very wide beamwidth antenna, any given magnitude and phase sample represents the sum return of all illuminated "points" on the ground of equal distance from the aircraft. Consequently, the resulting image will have very low resolution. SAR data processing must be performed to generate a high resolution SAR image.

Range Bins

$v_k(t_i) =$
Return from the kth transmitted pulse, where t is the time elasped since the pulse was transmitted

The samples from the most recent return are *stored* in the top row of the range bins. The data is *shifted* for each new pulse.

Azimuth Direction

Range Direction

Note: The Elasped Time t_i corresponds to a Range of R_i
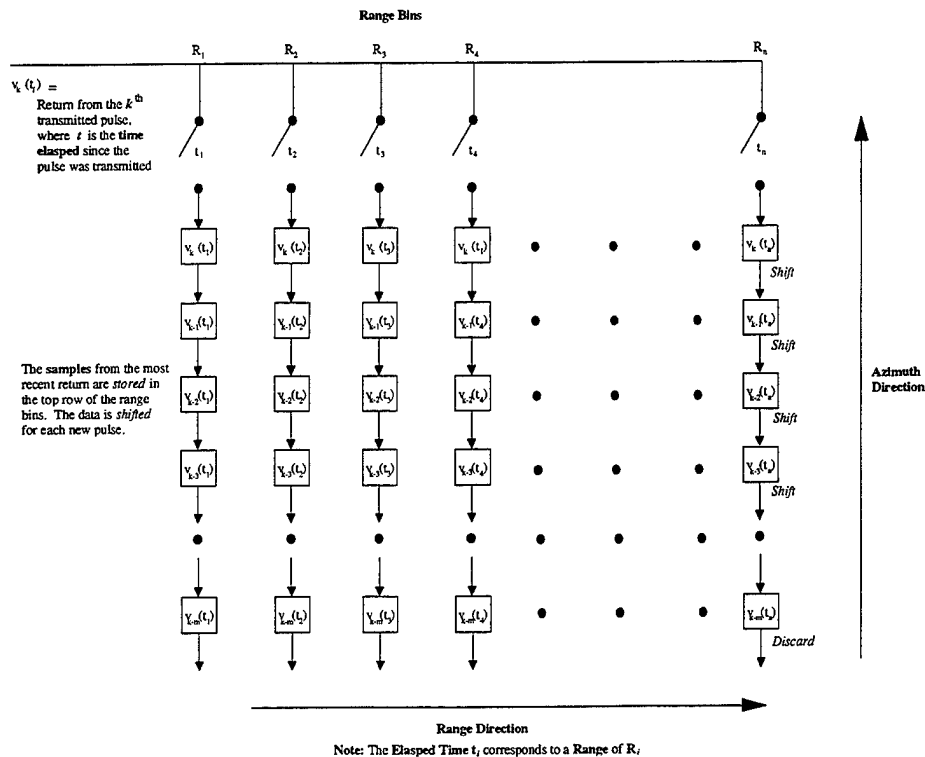
Figure 2. SAR Data Storage.

One method of SAR processing is called "unfocused line-by-line processing" (often call "**unfocused SAR**"). In unfocused SAR, the radar returns are thought of as a line of elemental radiators along the flight path. To synthesize a long array of antennas, a vector sum of the elements in each range bins is generated. This operation corresponds to the summing performed by the feed structure that interconnects the radiating elements of a real array.

Figure 3 illustrates the signal processing required for unfocused SAR. Note in Figure 3, that the magnitude of the vector sum is generated and then shifted onto the display memory. This process is repeated for every new radar pulse (or every i^{th} pulse for some systems), thus generating a real time high resolution image.

One major drawback of "unfocused SAR" is that it does not perform well when the image is generated at close ranges to the target area. In unfocused SAR, the length of the synthesized array of antennas must be short enough in relation to the range of the swath being mapped that the line of sight from any one point at the swath's range to the individual array elements are essentially parallel. As illustrated in Figure 4, if the "synthetic array length" is a significant fraction of the swath's range, then the range to a given point on the "synthetic array boresight" becomes different for each array element. These differences in range can result in considerable differences in the phase of the returns thus limiting the performance of the SAR. While the azimuth resolution can initially be reduced by increasing the length of the synthetic array, a point is soon reached which any further increase in length degrades the performance of the SAR.
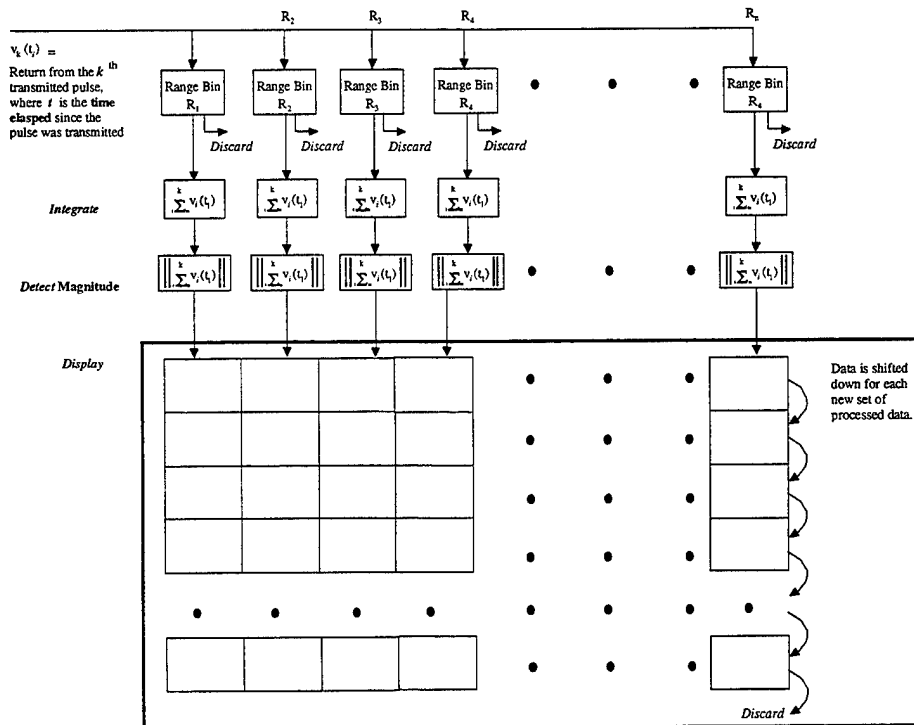
Figure 3. Unfocused line-by-line SAR data processing.
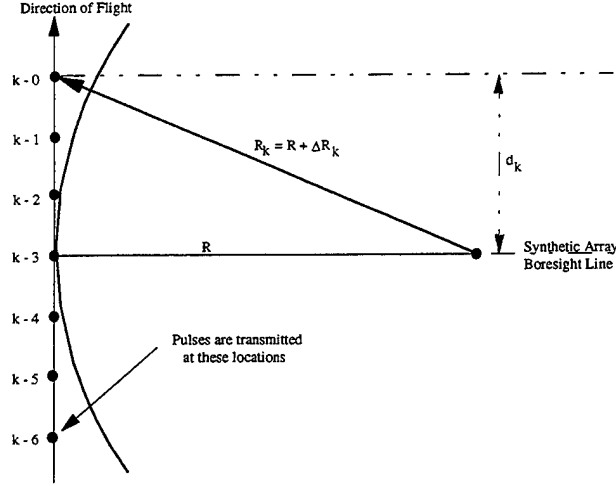
Figure 4. Distance variations for unfocused line-by-line processed SAR.

The limitation on array length of the unfocused SAR may be largely removed by "focusing" the synthetic array. Processing of this type is called "focused line-by-line processing" (often called "**focused SAR**"). In principle, focusing is achieved by simply applying the appropriate phase correction to the returns. For example, the necessary phase correction θ_k, for the kth radar pulse can be approximated as:

$$\theta_k \approx \frac{2\pi}{\lambda} (2\Delta R_k) \tag{3}$$

where λ is the wavelength of the transmitted pulse and ΔR_k is the range difference of the kth radar pulse to a point on the boresight when compared to the synthesized array boresight range. The ($2\Delta R_k$ term is used in Equation (3) to account for the round-trip travel of the radar pulse. Notice in Figure 3, that the following relationships exist:

$$(R + \Delta R_k)^2 = R^2 + d_k^2 \tag{4}$$

$$R^2 + 2R\Delta R_k + (\Delta R_k)^2 = R^2 + d_k^2 \tag{5}$$

$$2R\Delta R_k \left(1 + \frac{\Delta R_k}{2R}\right) = d_k^2 \tag{6}$$

$$\Delta R_k \approx \frac{d_k^2}{2R} \text{ for } \Delta R_k \ll 2R \tag{7}$$

where R is the synthetic boresight range and d_k is the distance of the kth pulse from the synthesized boresight. Substituting Equation (7) into Equation (3) yields the following approximation for the phase correction:

$$\theta_k \approx \frac{2\pi}{\lambda} \left(\frac{d_k^2}{R}\right). \tag{8}$$

6

Figure 5 illustrates the required processing for focused SAR. As the return from a transmitted pulse comes in, they are stored in the top row of the range bins. When the return for the last range bin has been received, the contents of every range bin is shifted down one row and the bottom range bin is discarded. Between these shifts, each range bin is read serially, appropriately "focused" (*phase shifted*) around the central array element, and summed. This focusing and summing process is often called "azimuth compression". As was performed for unfocused SAR, a magnitude is computed for the azimuth compression result. This magnitude is then shifted into the display memory.

One major drawback of unfocused line-by-line SAR processing is its computational complexity. Notice that every element of each range bin must be phase shifted and summed to generate a single line on the display. Every time the radar transmits a new pulse, it must perform a phase correction all over again. If the synthesized array is very long (many samples in a range bin), then computational requirements become immense.

The computational requirements can be reduced significantly by a SAR processing technique called "Doppler Processing". The computational burden is reduced by processing data in parallel for many lines of the image rather than one line at a time. In Doppler processing, the returns from different azimuth angles are isolated with Doppler filters.
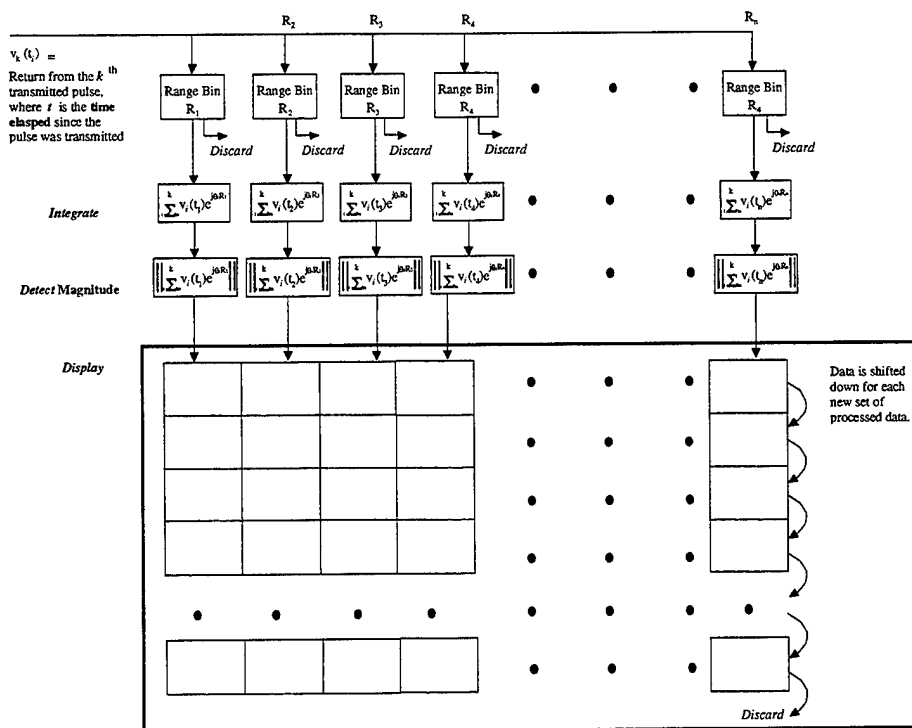
Figure 5. Focused line-by-line SAR processing.

To explain the details of this approach, first consider how Doppler frequency is related to the azimuth direction. As an aircraft approaches a point, the range is decreasing and the range rate is a negative value. When the aircraft is broadside of the target, the range rate becomes zero and then increases to a positive value as the aircraft begins to egress from the point. This fact is illustrated in Figure 6.
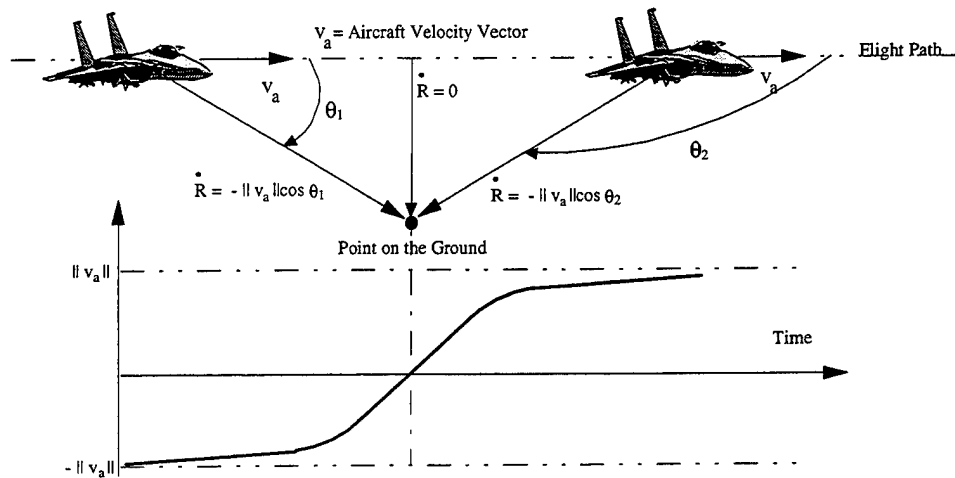
Figure 6. Doppler velocity of an aircraft as it passes a point on the ground.

The Doppler histories of several evenly spaced points at the same offset range is shown in Figure 7. As you can see, the Doppler histories are identical, except for being staggered slightly in time. Consequently, at any point in time, the return from every point has a slightly different frequency. The difference in frequency corresponds to an azimuth separation of the points. Therefore, by virtue of the differences in the Doppler shift, we can isolate the return received from each point.
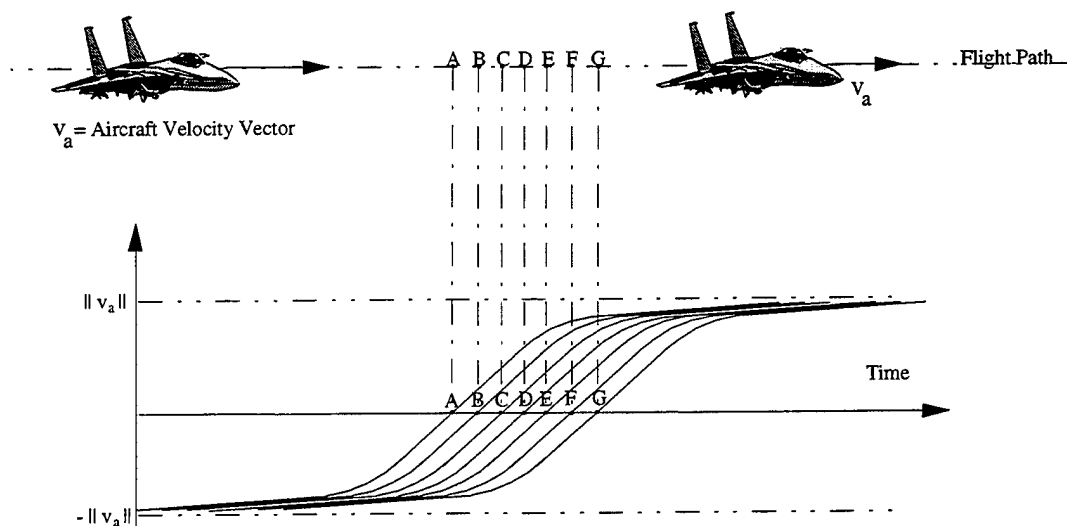
Figure 7. Doppler history of evenly spaced points on the ground.

Figure 8 illustrates, in block diagram form, how Doppler processing is performed. In Doppler processing, a phase correction is applied at the onset of data collection. This process, called focusing, converts the return from each point on the ground to a constant Doppler frequency. That frequency corresponds to the Doppler frequency, as seen from the center of the segment of flight over which radar return data was collected. When a complete set of data is collected in all range bins, the data is applied to a bank of Doppler filters which separates the azimuth components of the data. The magnitude of the result is then shifted into the display memory.
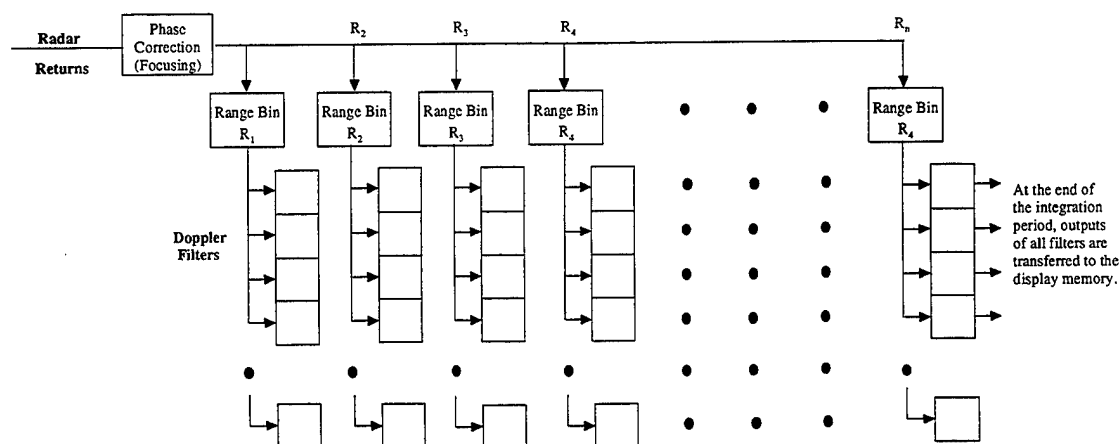
Figure 8. SAR Doppler processing.

Notice in Doppler processing that phase corrections are applied at two points in the processing algorithm, namely, when the return is focused and when the Doppler filtering is performed. For focusing, only one phase correction is required for each range bin element. The number of phase corrections needed for the back of Doppler filters is on the order of $N\log_2 N$, where N is the number of integrated radar returns. Thus, the total number of phase corrections required for Doppler processing is on the order of $N(1 + \log_2 N)$. It is easy to recognize that this value is somewhat less than the N^2 phase corrections needed for focused line-by-line SAR processing. Herein lies the major advantage of Doppler processing.

The SAR processing techniques above have been presented with the assumption of *stripmap* **mode SAR**. Stripmap SAR is simply a side-looking radar that maps a strip of area on the ground parallel to the flight path. However, by gradually changing the look angle of the real antenna as the aircraft travels, the radar can repeatedly map a given region of interest. This mode of operation, called *spotlight mode* **SAR**, enables the operator to maintain surveillance over an area for a longer period of time. Also, since the beam dwells continually over the mapped area, the length of the synthetic array is not limited by the real antenna beamwidth. Consequently, spotlight SAR is capable of generating superior quality images. Figure 9 illustrates the differences between stripmap mode SAR and spotlight mode SAR.
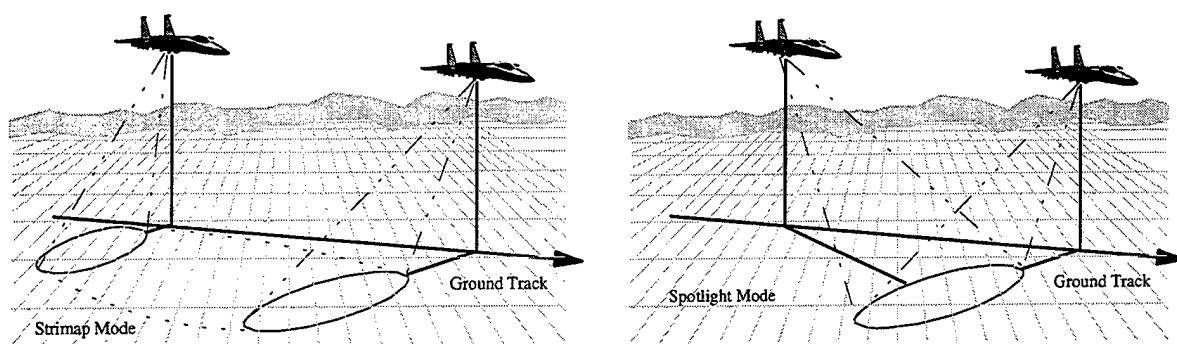
Figure 9. **Stripmap mode** SAR versus **spotlight mode** SAR.

3.0 Monopulse Radar Background

A monopulse radar measures the azimuth and elevation angles of the line-of-sight vector from the aircraft to the target. The basic vector geometry defining the azimuth angle (A) and elevation (E) angle are shown in Figure 10. Here, the azimuth angle is defined to be the angle between a vector pointing along the antenna frame y-axis and the line-of-sight vector. The elevation angle is defined to be the angle between a vector pointing along the antenna frame z-axis and the line-of-sight vector. The antenna frame is defined in detail in the next section of this report.
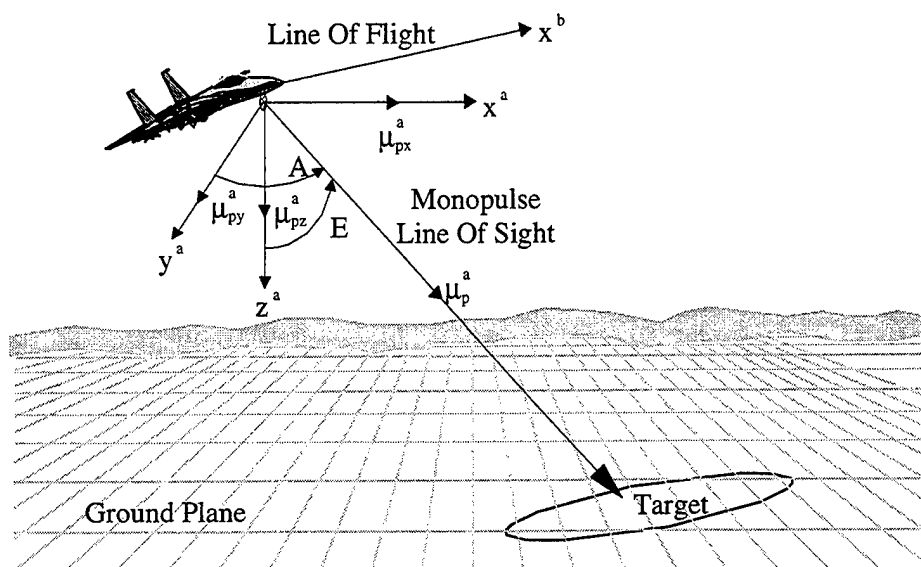
Figure 10. SAR Geometry.

The term monopulse refers to the ability of the radar to obtain complete angle information from a single radar pulse. In a monopulse radar, a pair of antennas is used to form two similar beams which point in slightly different directions. These two antenna ports are connected to a hybrid, a device for combining the receiver RF signals, to obtain a sum and difference output. The antenna pattern for the difference port will exhibit a null directly between the beams. Likewise, the pattern for the sum port will exhibit peak directly between the beams. This makes possible a pencil-beam tracking and/or angle measurement radar that exhibits very high precision.

Many SAR systems include a monopulse radar mode. In operation, the monopulse processor measures the azimuth and elevation angles for every cell in the SAR image.

11

4.0 Measurement Geometry

In this section, the coordinate frames are defined and the coordinate transformation matrices are developed. Also, this section summarizes some basic geometric relationships for SAR range and range rate measurements and monopulse radar azimuth and elevation measurements.

4.1 Coordinate Frames

The coordinate systems of interest for this problem are the Earth-centered Earth-fixed (ECEF) frame, the navigation frame, the heading frame, the path frame, the body frame, and the antenna frame. These right handed orthogonal coordinate frames are defined below. Refer to Figure 11 for a graphical interpretation of each of these frames.

1) Earth centered fixed frame (x^e, y^e, z^e):

As the name suggests, the ECEF frame has its origins at the Earth's center of mass. The z^e axis is the Earth's axis of rotation and points toward the north pole. The x^e - ye axis lies in the Earth's equatorial plane such that x^e is fixed at Greenwich.

2) Navigation frame (x^n, y^n, z^n):

The navigation frame has its origins at the aircraft's center with the x^n-y^n plane tangent to the reference ellipsoids (i.e. the navigation frame is a local level frame). In this frame, x^n points north, y^n points east, and z^n points down perpendicular to the reference ellipsoid. The location of the navigation frame is typically specified relative to the ECEF frame by the longitude λ, the latitude ϕ, and the altitude h.

3) Heading frame (x^h, y^h, z^h):

The heading frame is local level frame whose origin is located at the aircraft's center. The x^h axis points in the direction of the local level component of the velocity vector. The z^h axis points down toward the reference ellipsoid and the y^h is tangent to the reference ellipsoid. As shown in Figure 11(b), the heading frame is defined relative to the navigation frame by a rotation, denoted η_z, about the z^h axis.

4) Path frame (x^p, y^p, z^p):

The path frame has its origins at the aircraft's center such that the x^p axis points in the direction of the velocity vector. The y^p axis is tangent to the reference ellipsoid and points in the same direction as y^h. The z^p point in an appropriate direction for a right-handed orthogonal coordinate frame. Note in Figure 11C, the path is defined relative to the heading frame by a rotation, denoted η_y, about the y^h axis.

5) Body frame (x^b, y^b, z^b):

As depicted in Figure 11D, the body frame defines the attitude of the aircraft's body relative to the navigation frame via roll, and yaw angles α_x, α_y, and α_z. Its origin is at the aircraft's center such that x^b points out the nose of the aircraft, y^b points out the right side of the aircraft, and z^b points out the bottom of the aircraft.

6) Antenna frame (x^a, y^a, z^a):

The antenna frame defines the orientation of the radar's antenna relative to the body frame via antenna roll angles ς_x, antenna pitch angle ς_y, and antenna yaw angle ς_z. The antenna frame x^a axis is defined such that it points in a direction perpendicular to the antenna phase plane. The y^a axis and z^a both lie in the phase plane of the antenna such that y^a points along the semi-minor axis and z^a points along the semi-major axis. The origin of the antenna frame is assumed to be at the aircraft's center.

4.2 Coordinate Transformations

Coordinate transformations between frames are often required to perform vector additions and multiplications. The necessary coordinate transformations are summarized below. In order to write the results compactly, we abbreviated cos by C and sin by S.

Navigation frame to ECEF frame

$$C_n^e = \begin{bmatrix} -S\phi C\lambda & -S\lambda & -C\phi C\lambda \\ -S\phi S\lambda & C\lambda & -C\phi S\lambda \\ C\phi & 0 & -S\phi \end{bmatrix} \tag{9}$$

Heading frame to navigation frame

$$C_h^n = \begin{bmatrix} C\eta_x & -S\eta_x & 0 \\ S\eta_x & C\eta_x & 0 \\ 0 & 0 & 1 \end{bmatrix} \tag{10}$$

Path frame to heading frame

$$C_p^h = \begin{bmatrix} C\eta_y & 0 & S\eta_y \\ 0 & 1 & 0 \\ -S\eta_y & 0 & C\eta_y \end{bmatrix} \tag{11}$$

Body frame to navigation frame

$$C_b^n = \begin{bmatrix} C\alpha_z C\alpha_y & C\alpha_z S\alpha_y S\alpha_x - S\alpha_z C\alpha_x & C\alpha_z S\alpha_y C\alpha_x + S\alpha_z S\alpha_x \\ S\alpha_z C\alpha_y & S\alpha_z S\alpha_y S\alpha_x + C\alpha_z C\alpha_x & S\alpha_z S\alpha_y C\alpha_x - C\alpha_z S\alpha_x \\ -S\alpha_y & C\alpha_y S\alpha_x & C\alpha_y C\alpha_x \end{bmatrix} \tag{12}$$

Antenna frame to body frame

$$C_a^b = \begin{bmatrix} C\varsigma_z C\varsigma_y & C\varsigma_z S\varsigma_y S\varsigma_x - S\varsigma_z C\varsigma_x & C\varsigma_z S\varsigma_y C\varsigma_x + S\varsigma_z S\varsigma_x \\ S\varsigma_z C\varsigma_y & S\varsigma_z S\varsigma_y S\varsigma_x + C\varsigma_z C\varsigma_x & S\varsigma_z S\varsigma_y C\varsigma_x - C\varsigma_z S\varsigma_x \\ -S\varsigma_y & C\varsigma_y S\varsigma_x & C\varsigma_y C\varsigma_x \end{bmatrix} \qquad (13)$$
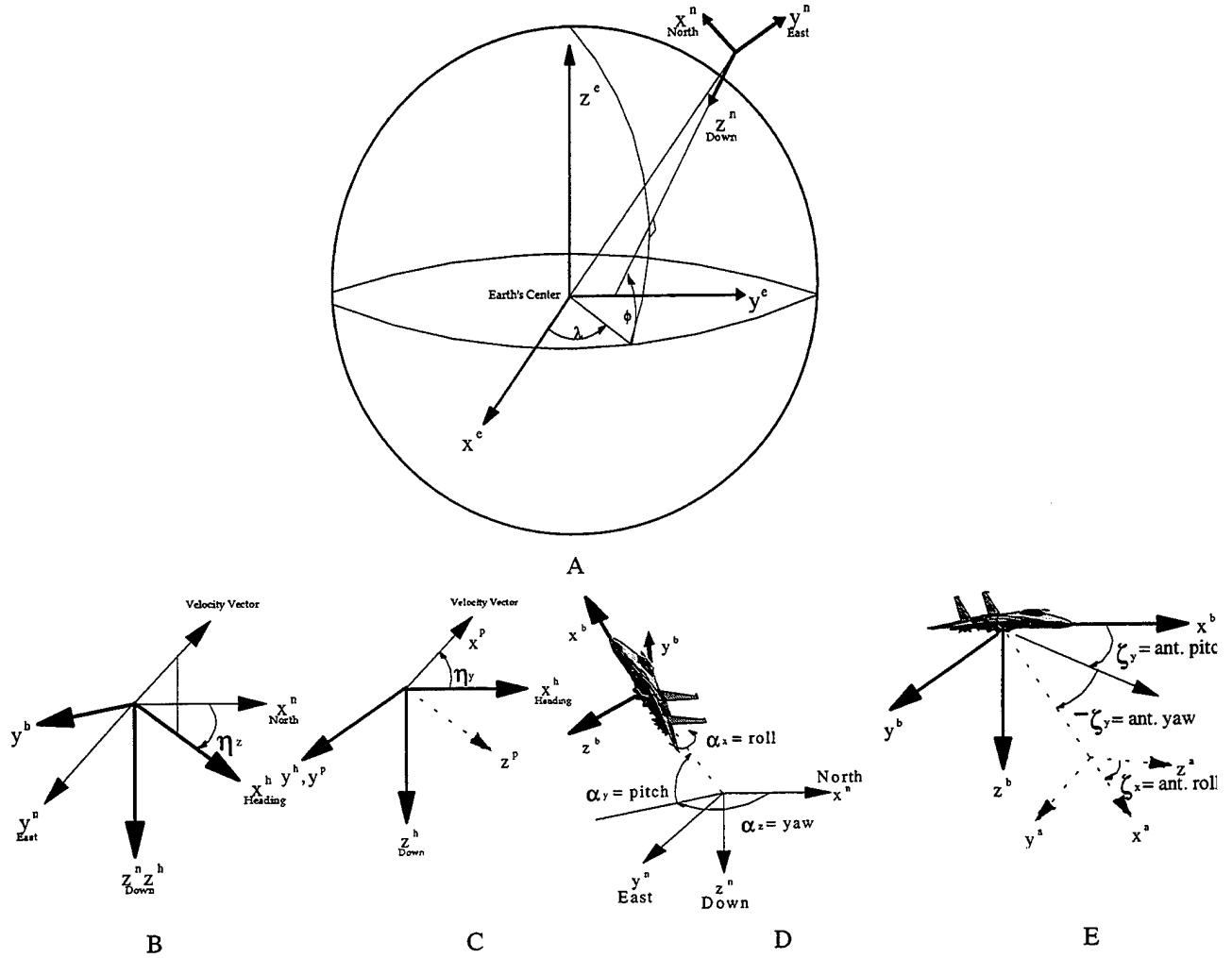
Figure 11. Graphical Depiction of the Euler angles between, A) the navigation and ECEF frames; B) the heading frame and the navigation frame; C) the path frame and the heading frame; D) the body and navigation frames; and E) the antenna and body frames. Note in (D) and (E), the frames were separated for clarity.

4.3 Geometry of SAR Range and Range Rate Measurements

The basic vector geometry of an aircraft and a ground based target in an Earth-center fixed (ECEF) coordinate is shown in Figure 12.

The relationship between the ECEF referenced line-of-sight vector $\mathbf{p}^e$, the target location vector $\mathbf{r}_t^e$, and the aircraft position vector, $\mathbf{r}_a^e$, is given by:

$$\mathbf{p}^e = \mathbf{r}_t^e - \mathbf{r}_a^e \qquad (14)$$

The **range** from the aircraft to the target is the magnitude of $\mathbf{p}$ which is found by computing the 2-norm of the vector.

$$r = \|\mathbf{p}^e\| = \sqrt{[(\mathbf{p}^e)^T \mathbf{p}^e]} \qquad (15)$$
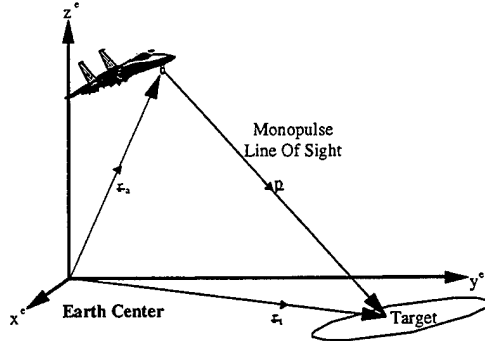
Figure 12. Target Location Geometry.

The **range rate** is found by computing the time derivative of r.

$$\dot{r} = \frac{dr}{dt} = \frac{(\mathbf{p}^e)^T \frac{d\mathbf{p}^e}{dt}}{\sqrt{[(\mathbf{p}^e)^T \mathbf{p}^e]}} \qquad (16)$$

For stationary targets, which we now assume, note that the term, $\frac{d\mathbf{p}^e}{dt}$, in Equation (16) becomes:

$$\frac{d\mathbf{p}^e}{dt} = \frac{d\mathbf{r}_t^e}{dt} - \frac{d\mathbf{r}_a^e}{dt} = -\mathbf{v}_a^e \qquad (17)$$

where $\mathbf{v}_a^e$, is the Earth-referenced aircraft velocity expressed in the Earth frame. Also, note that the unit look vector $\mathbf{u}_p^e$ between the aircraft and the ground target may be expressed as:

$$\mathbf{u}_p^e = \frac{\mathbf{p}^e}{\|\mathbf{p}^e\|} = \frac{\mathbf{p}^e}{\sqrt{[(\mathbf{p}^e)^T \mathbf{p}^e]}} \qquad (18)$$

Substituting Equations (17) and (18) into Equation (16) yields the following expression for the range rate:

$$\dot{r} = -(\mathbf{u}_p^e)^T \mathbf{v}_a^e \qquad (19)$$

It is easily shown that Equations (15) and (19) can be expressed directly in terms of the navigation frame vectors, i.e.:

$$r = \|\mathbf{p}^n\| = \sqrt{[(\mathbf{p}^n)^T \mathbf{p}^n]} \qquad (20)$$

$$\dot{r} = -(\mathbf{u}_p^n)^T \mathbf{v}_a^n \tag{21}$$

4.4 Geometry of Monopulse Radar Azimuth and Elevation Angle Measurements

Recall that the geometry defining the azimuth angle (A) and elevation (E) angle is shown in Figure 10 above. Consider the unit vectors $\mathbf{u}_{py}^a$ and $\mathbf{u}_{pz}^a$ which point in the y^a and z^a directions, respectively. These vectors are expressed in the antenna coordinates as

$$\mathbf{u}_{py}^a = [\,0 \;\; 1 \;\; 0\,]^T \tag{22}$$

$$\mathbf{u}_{pz}^a = [\,0 \;\; 0 \;\; 1\,]^T \tag{23}$$

and may be converted to the navigation frame by employing coordinate transformations:

$$\mathbf{u}_{py}^n = C_b^n\, C_a^b\, \mathbf{u}_{py}^a = C_a^n\, \mathbf{u}_{py}^a \tag{24}$$

$$\mathbf{u}_{pz}^n = C_b^n\, C_a^b\, \mathbf{u}_{pz}^a = C_a^n\, \mathbf{u}_{pz}^a \tag{25}$$

The relationship between A and E (quantities measured by the radar) and the unit vectors of interest are given by:

$$\cos(A) = (\mathbf{u}_p^n)^T\, \mathbf{u}_{py}^n \tag{26}$$

$$\cos(E) = (\mathbf{u}_p^n)^T\, \mathbf{u}_{pz}^n \tag{27}$$

Solving for A and E yields

$$A = \cos^{-1}\left[(\mathbf{u}_p^n)^T\, \mathbf{u}_{py}^n\right] \tag{28}$$

$$E = \cos^{-1}\left[(\mathbf{u}_p^n)^T\, \mathbf{u}_{pz}^n\right] \tag{29}$$

where both A and E lie in the interval $[0, \pi]$ radians.

5.0 Targeting with SAR Measurements

In general, SAR targeting algorithms need three pieces of information to compute a target's location, namely range, range rate, and height above the target. As shown in Figure 13, the intersection of the sphere of constant range, cone of constant range rate (centered about the aircraft velocity vector), and the plane of constant height above target defines the location of the target.
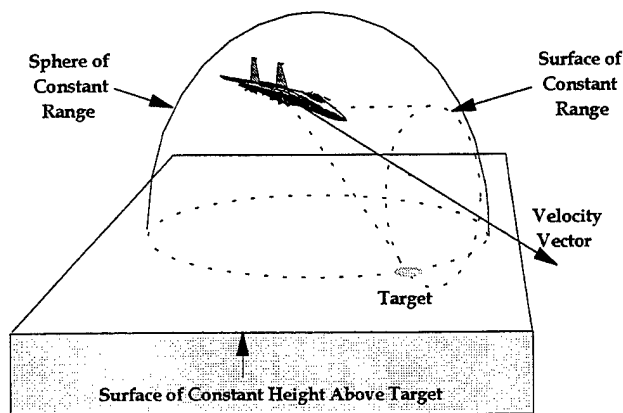
Figure 13. Range-Doppler target location geometry.

Range and range rate are inherently measured and stored for each cell in a Doppler processed SAR image. The height above target, can be computed from the range measurement and the precise angle measurements of a monopulse radar. Derived next are the mathematical equations needed to solve the target's location form radar measurements. For the development which follows refer to Figure 14.
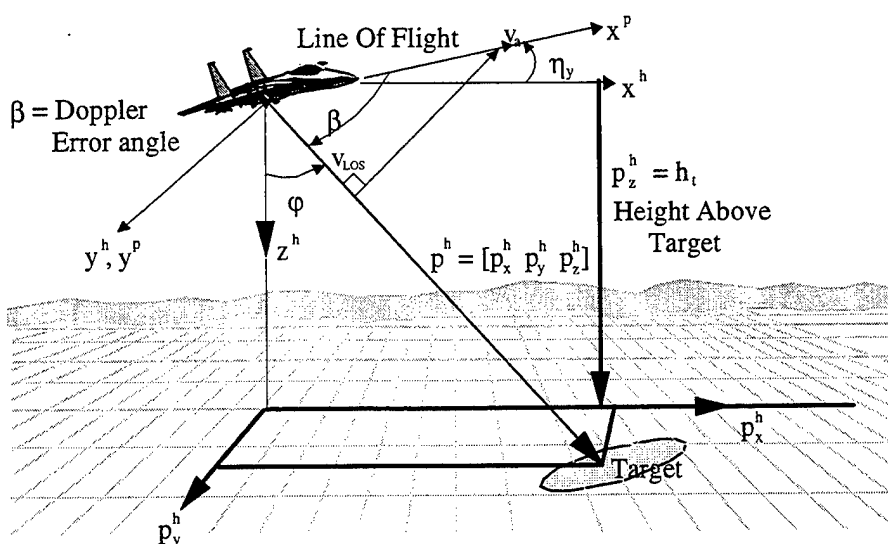
Figure 14. Graphical depiction of SAR targeting.

Here we consider the target's location vector in path frame coordinates. Notice that Doppler cone angle, β, is the direction cosine of the line-of-sight (LOS) vector relative to the x-axis of the path frame. Therefore, the following relationship exists between the Doppler cone angle and the x component of the LOS vector

$$\cos(\beta) = \frac{p_x^p}{r} \tag{30}$$

Solving for the p_x^p yields

$$p_x^p = r \cos(\beta) \tag{31}$$

Note that if $\beta \leq \pi/2$, the $\cos(\beta)$ can be computed by the following equation:

$$\cos(\beta) = \frac{|v_{LOS}|}{|v_a|} \tag{32}$$

where $|v_{LOS}|$ is the component of the Earth reference velocity v_a along the radar line-of-sight. Recognizing the fact that $|v_{LOS}| = |\dot{r}|$ and substituting Equation (32) into (31) yields the following expression for the x-component of p^p

$$p_x^p = r \left[\frac{|\dot{r}|}{|v_a|} \right] \tag{33}$$

The y-component of p^p is derived using the trigonometric identity, $\sin^2(\beta) = 1 - \cos^2(\beta)$, and Equation (30) to obtain the following expression:

$$\sin^2(\beta) = 1 - \frac{(p_x^p)^2}{r^2} \tag{34}$$

$$\sin^2(\beta) = 1 - \frac{(p_x^p)^2}{(p_x^p)^2 + (p_y^p)^2 + (p_z^p)^2} \tag{35}$$

$$\sin^2(\beta) = \frac{(p_y^p)^2 + (p_z^p)^2}{(p_x^p)^2 + (p_y^p)^2 + (p_z^p)^2} \tag{36}$$

$$\sin^2(\beta) = \frac{(p_y^p)^2 + (p_z^p)^2}{r^2} \tag{37}$$

Solving for $(p_y^p)^2$:

$$(p_y^p)^2 = \sqrt{r^2 \sin^2(\beta) - (p_z^p)^2} \tag{38}$$

$$(p_y^p)^2 = \sqrt{r^2 (1 - \cos^2(\beta)) - (p_z^p)^2} \tag{39}$$

$$(p_y^p)^2 = \sqrt{r^2 \left\{ 1 - \left[\frac{|\dot{r}|}{|v_a|} \right]^2 \right\} - (p_z^p)^2} \qquad (40)$$

In Equations (33) and (40), we now have expressions for the path frame x and y components of the LOS vector. The known quantities in these equations are the range, r, and the range rate, $\dot{r}$, (measured by the SAR) and the aircraft velocity vector v_a (measured by the inertial navigation system). The unknown terms are the components of the target location vector, p_x^p, p_y^p, and p_z^p. Hence, we have two equations and three unknowns. To find the third equation needed to solve the target's location, we must also consider the heading frame coordinates.

Note in Figure 14, that the heading frame z-component of the LOS vector is equal to the height above the target measurement such that

$$p_z^h = h_t \qquad (41)$$

Also, recall that the heading frame coordinates are related to the path frame coordinates by a simple coordinate transformation, i.e.

$$p_x^h = \cos(\eta_y) \, p_x^p + \sin(\eta_y) \, p_z^p \qquad (42)$$

$$p_y^h = p_y^p \qquad (43)$$

$$p_z^h = -\sin(\eta_y) \, p_x^p + \cos(\eta_y) \, p_z^p \qquad (44)$$

From Equations (41) and (44) it is easily shown that the path frame z-component of the LOS vector is given by the following expressions:

$$p_z^p = \frac{1}{\cos(\eta_y)} \left[\sin(\eta_y) \, p_x^p + h_t \right] \qquad (45)$$

$$p_z^p = \tan(\eta_y) \, p_x^p + \frac{h_t}{\cos(\eta_y)} \qquad (46)$$

$$p_z^p = \tan(\eta_y) \, r \left[\frac{|\dot{r}|}{|v_a|} \right] + \frac{h_t}{\cos(\eta_y)} \qquad (47)$$

Using the results derived in Equations (33), (40), and (47); the overall vector p^p is expressed as:

$$\mathbf{p}^p = \begin{bmatrix} p_x^p \\ p_y^p \\ p_z^p \end{bmatrix} = \begin{bmatrix} r\left[\dfrac{|\dot{r}|}{|v_a|}\right] \\ \sqrt{r^2\left\{1-\left[\dfrac{|\dot{r}|}{|v_a|}\right]^2\right\} - \left[\tan(\eta_y)\, r\left[\dfrac{|\dot{r}|}{|v_a|}\right] + \dfrac{h_t}{\cos(\eta_y)}\right]^2} \\ \tan(\eta_y)\, r\left[\dfrac{|\dot{r}|}{|v_a|}\right] + \dfrac{h_t}{\cos(\eta_y)} \end{bmatrix} \qquad (48)$$

The terms $\cos(\eta_y)$ and $\sin(\eta_y)$ in Equations (48) are found by using the INS indicated velocities in the following equations:

$$\cos(\eta_y) = \frac{v_x^h}{|v_a|} \qquad (49)$$

$$\tan(\eta_y) = -\frac{-v_z^h}{v_x^h} \qquad (50)$$

where v_x^h and v_z^h are the heading frame x and y components, respectively, of the aircraft velocity vector. Next we consider the computation of the height above target, h_t, from monopulse radar angle measurements.

Given the monopulse radar measurements of azimuth and elevation angle, it is possible to compute a unit LOS vector, $\mathbf{u}_p^a$, in antenna coordinates. This is done with the following equations:

$$\mathbf{u}_{px}^a = \sqrt{1 - \cos^2(A) - \cos^2(E)} \qquad (51)$$

$$\mathbf{u}_{py}^a = \cos(A) \qquad (52)$$

$$\mathbf{u}_{pz}^a = \cos(E) \qquad (53)$$

where $\mathbf{u}_p^a = [\mathbf{u}_{px}^a \ \mathbf{u}_{py}^a \ \mathbf{u}_{pz}^a]^T$. This antenna frame unit vector may be expressed in navigation frame coordinates by employing the appropriate coordinate transformations, i.e.

$$\mathbf{u}_p^n = C_b^n\, C_a^b\, \mathbf{u}_p^a. \qquad (54)$$

Notice, that the vector $\mathbf{u}_p^n$ is also a unit vector. Consequently, the component of $\mathbf{u}_p^n$ are the direction cosines angles (i.e. the cosine of the angles between the navigation frame coordinate axes and the line-of-sight vector, denoted $\cos(\varphi)$. Using this fact it is easily shown that the height above the target is given by:

$$h_t = r\cos(\varphi) = r\,\mathbf{u}_{pz}^n \qquad (55)$$

where $\mathbf{u}_{pz}^n$ is the z-component of $\mathbf{u}_p^n$.

As shown in this section, it is possible to compute a target's location using only one set of SAR and monopulse radar measurements. When a Kalman filter is used with multiple-look measurements, it may be possible to locate

a target with a smaller set of measurements (e.g. range measurements only). Also, by utilizing the complete measurement history, a Kalman filter, provides a means to continually improve the estimate of the target's location.

6.0 Radar Measurement Models

In this section, we present the measurement equations for both the SAR and monopulse radar measurements. Here, we describe the different sources of errors present in each measurement. Also, each error is characterized by a Stochastic model so that they may be incorporated in a Kalman filter design.

6.1 SAR Measurements

As previously mentioned, a SAR is capable of measuring range and range rate to a given target. However, these measurements are not perfect and must be modeled as the sum of true value and the measurement errors and noises. The measured range, denoted $\tilde{r}$, and range rate, denoted $\tilde{\dot{r}}$, are modeled by the following equations:

$$\tilde{r} = r + \delta r_{CL} + r\delta C - v_{r_{DES}} - v_{r_Q} - v_{r_T} - v_{r_{OT}} \tag{56}$$

$$\tilde{\dot{r}} = \dot{r} + \delta \dot{r}_D + \dot{r}\delta C + \dot{r}\delta F - v_{\dot{r}_{DES}} - v_{\dot{r}_Q} - v_{\dot{r}_T} - v_{\dot{r}_{OT}} \tag{57}$$

where

δr_{CL} is the range clock (phase) error,

$\delta \dot{r}_D$ is a Doppler measurement error,

δC is the radar wave propagation speed error

δF is the radar frequency error

$v_{r_{DES}}$ is the range designation error

$v_{\dot{r}_{DES}}$ is the range rate designation error

v_{r_Q} is the range quantization error

$v_{\dot{r}_Q}$ is the range rate quantization error

v_{r_T} is the range timing error

$v_{\dot{r}_T}$ is the range rate timing error

$v_{r_{OT}}$ is range error which captures the effects of multipath, high maneuvers, and edge of map targeting

$v_{\dot{r}_{OT}}$ is range rate error capturing the effects of multipath, high maneuvers, and edge of map targeting.

Other potential range rate measurement errors, which are not modeled here, include the errors associated with wave movement when targeting is performed over bodies of water. Presented next is a brief description of each error source.

22

Range measurements are made by measuring the time difference between the transmitted pulse and its return. Consequently, any error found in the clock rate will result in a range measurement error. In general, a clock runs either slightly fast or slightly slow with very slowly changing variations in the rate. Therefore, the error δr_{CL} in the range measurement resulting from a clock error is modeled here as a random bias, i.e.

$$\dot{\delta r}_{CL} = 0 \qquad (58)$$

The rms value of this error is on the order of 0.01 feet.

Recall that the radar measures range rate by measuring the Doppler frequency of return pulses. However, some radar system can induce Doppler frequency shifts when transmitting radar pulses and when receiving the return. This results in an error in the range rate measurement. The error $\delta \dot{r}_D$ in the range rate measurement resulting from system induced Doppler shift error is modeled here as a random bias, i.e.,

$$\dot{\delta \dot{r}}_D = 0 \qquad (59)$$

The rms value of this error is on the order of 0.001 feet/sec.

Knowledge of the radar wave propagation speed is needed to map the measured radar wave transit time to a range measurement and the measured Doppler frequency to the radar range rate measurement. Therefore, as shown in Equations (56) and (57), the propagation speed error has "scale factor" type effect on both the range and the range rate measurements. Likewise, since knowledge of the radar frequency is needed to map Doppler frequency to a range rate measurement, error in the radar pulse frequency will also have a scale factor effect on the range rate measurement.

The propagation speed error, $\dot{\delta C}$, and frequency error, δF, are modeled here as random bias, i.e.

$$\dot{\delta C} = 0 \qquad (60)$$

$$\dot{\delta F} = 0 \qquad (61)$$

The rms value of the propagation speed error is on the order of 10 PPM. The rms value of the frequency error is on the order of 20 PPM.

The target designation error results from the human operator's inability to designate the exact pixel in the SAR image that represents the desired target. The target designation error can be modeled as a function of four parameters, namely clutter-to-noise (CNR), signal-to-noise (SNR), signal-to-clutter-plus noise ratio (SCNR), and the resolution cell size. The CNR establishes that the image quality is sufficient for individual fixed targets to be designated. If the CNR is less than 3 dB, the variance of the target designation error in both the range and azimuth directions is assumed large. The SCNR is compared to a threshold of (10dB) to establish that the

23

individual targets are recognizable by a human operator. The CNR, SNR, and SCNR are characterized by the following expressions:

$$\text{CNR} = \rho_c \Delta G^2 L_a L_r T_1 \frac{r_o}{r} \tag{62}$$

$$\text{SNR} = \rho_t \Delta G^2 L_a L_r T_1 \left(\frac{r_o}{r}\right)^4 \tag{63}$$

$$\text{SCNR} = \frac{\text{SNR}}{\text{CNR} + 0.1} \tag{64}$$

where

$$L_a = 10^{(2.16 \times 10^{-6})r} = atmospheric\ loss \tag{65}$$

$$L_r = 10^{(5.4 \times 10^{-6})\eta r} = rain\ attention \tag{66}$$

$$\rho_c = 0.1(\Delta r)(\Delta az) = clutter\ cross\text{-}section \tag{67}$$

and where T_1 is the SAR integration time ΔG^2 is the two way loss in the mainlobe gain, ρ_t, is the target cross-sectional area, η is the rain rate in mm/hr, r is the range to the target, Δr and Δaz are the azimuth and range resolutions, respectively, and r_o is the range at which the SNR is unity for 1 m^2 target, 1 sec array time, and undegraded mainlobe antenna gain. A typical value of r_o is 1.5 x 10^5 m. For a stripmap SAR, range and azimuth resolutions are given in [9] by the following expressions:

$$\Delta r = \frac{c}{2B} = \frac{c\tau}{2} \tag{68}$$

$$\Delta az = \frac{D}{2} \tag{69}$$

respectively, where c is the speed of light, B is the bandwidth of the transmitted pulse, τ is the unmodulated pulse length, and D is the antenna diameter. For a spotlight mode SAR, the range resolution is the same as above and the azimuth resolution is expressed as:

$$\Delta az = \frac{\lambda}{2\phi} \tag{70}$$

where λ is the wavelength of the transmitted pulse, and ϕ is the angle between the aircraft and the target created by the motion of the aircraft during SAR image data collection.

In earlier discussion SAR processing, it was shown that the range rate measurement is directly related to the azimuth direction of the SAR image. Consequently, the range rate resolution, denoted Δr, is a function of the azimuth resolution. In [9], this relationship is given by the following equation

$$\Delta \dot{r} = \omega_t \Delta az \tag{71}$$

24

where ω_t is the angular "rotation rate" of the aircraft around the target. The angular rotation rate is given by the following equation:

$$\omega_t = \frac{|v_a^n|}{r}\sqrt{\left[1 - \frac{|\dot{r}|}{|v_a|}\right]^2} \tag{72}$$

When the (SCNR > 10 dB), the designation error is often modeled as white noise with a range component, denoted $v_{r_{DES}}$, and a range rate components, denoted $v_{\dot{r}_{DES}}$. The rms value for the range and the range rate components are given by:

$$rms\ value\ for\ v_{r_{DES}} = K\Delta r \tag{73}$$

$$rms\ value\ for\ v_{\dot{r}_{DES}} = K\Delta \dot{r} \tag{74}$$

respectively, where typical values of K are on the interval [0.2, 2.5]. Generally, K is inversely proportional to the SCNR. In [2], K is modeled by the following expression:

$$K = \frac{1}{2\sqrt{SCNR}} \tag{75}$$

Here, we will model K as a constant of value 2.0.

The range quantization error, v_{r_Q}, and the range rate quantization errors, $v_{\dot{r}_Q}$ are a result of range and range rate resolution errors. In [10], quantization error is modeled as a uniformly distributed white noise. Therefore, the range and range rate quantization error are modeled as white noises with an rms value equal to the following:

$$rms\ value\ for\ v_{r_Q} = \frac{\Delta r}{\sqrt{12}} \tag{76}$$

$$rms\ value\ for\ v_{\dot{r}_Q} = \frac{\Delta \dot{r}}{\sqrt{12}} \tag{77}$$

The range timing error, v_{r_T}, and the range rate timing error $v_{\dot{r}_T}$, result from the time delay needed to perform SAR processing. These timing errors are modeled as white noises with rms values given by the following expressions

$$rms\ value\ for\ v_{r_T} = T_d\, r \tag{78}$$

$$rms\ value\ for\ v_{\dot{r}_T} = T_d\, \dot{r} \tag{79}$$

respectively, where T_d is the delay time. The time delay for this process is on the order of 1 ms.

The white noise errors, $v_{r_{OT}}$, and $v_{\dot{r}_{OT}}$, are added to the range and range rate measurements, respectively, to capture the effects of other miscellaneous sources. Such errors included high maneuver, edge of map targeting, signal multipath, and small squint angles. These errors are not always present in the SAR measurements. The lump sum effect of these errors are modeled here as white noises with rms values given by the following equation:

$$rms\ value\ for\ v_{r_{OT}} = 0.5\Delta r \tag{80}$$

$$rms\ value\ for\ v_{\dot{r}_{OT}} = 0.5\Delta \dot{r} \tag{81}$$

6.2 Monopulse Radar Measurements

Recall that monopulse radar is capable of measuring the azimuth angle, A, and the elevation angle E. Similar to the SAR measurements, the monopulse radar measurements are also corrupted by a number of errors. As a result, they may be expressed as the sum of the true value and the measurement errors.

For an electronically scanned array antenna (ESA), which we now assume, the measured azimuth angle, denoted $\tilde{A}$, and elevation angle, denoted $\tilde{E}$, are modeled by the following equations:

$$\tilde{A} = A + \delta A_{TEMP} - v_{A_{MA}} - v_{A_{FL}} - v_{A_{PU}} - v_{A_{CC}} - v_{A_{MS}} - v_{A_{TN}} - v_{A_Q} - v_{A_{RAD}} \tag{82}$$

$$\tilde{E} = E + \delta E_{TEMP} - v_{E_{MA}} - v_{E_{FL}} - v_{E_{PU}} - v_{E_{CC}} - v_{E_{MS}} - v_{E_{TN}} - v_{E_Q} - v_{E_{RAD}} \tag{83}$$

where

δA_{TEMP} and δE_{TEMP} are the temperature induced errors

$v_{A_{MA}}$ and $v_{E_{MA}}$ are the mechanical alignment errors

$v_{A_{FL}}$ and $v_{E_{FL}}$ are the flexure errors

$v_{A_{PU}}$ and $v_{E_{PU}}$ are the phase uniformity errors,

$v_{A_{CC}}$ and $v_{E_{CC}}$ are the Rx channel cross coupling terms

$v_{A_{MS}}$ and $v_{E_{MS}}$ are the monopulse slope errors,

$v_{A_{TN}}$ and $v_{E_{TN}}$ are the thermal noise errors

v_{A_Q} and v_{E_Q} are the measurement quantization errors,

$v_{A_{RAD}}$ and $v_{E_{RAD}}$ are the random deflection errors.

Other potential errors in the azimuth and elevation angle measurement, which are not modeled here, include atmospheric bending effects. Presented next is a brief description of each of the above errors.

The **temperature errors**, δA_{TEMP} and δE_{TEMP}, result from a temperature gradient across the face of the antenna array. The antenna temperature induced errors are modeled as biases, i.e.

$$\dot{\delta A}_{TEMP} = 0 \tag{84}$$

$$\dot{\delta E}_{TEMP} = 0 \tag{85}$$

26

The rms value for the temperature induced errors are on the order of 0.4 mrads.

To increase the potential scan area, many SAR antennas are designed so that they are steered both electronically and mechanically. In this case, there will be pointing errors resulting from inaccuracies in both the electronic and mechanical steering mechanisms. The errors, $v_{A_{MA}}$ and $v_{E_{MA}}$, are a result of **mechanically steering errors**. Other errors in this section capture the effects of electronics steering inaccuracies. The mechanical alignment errors are modeled here as white noise with an rms value on the order of 0.3 *mrads*.

The **flexure errors**, $v_{A_{FL}}$ and $v_{E_{FL}}$, model the effects of structure vibrations and bending between the antenna and the body of the aircraft. The flexure errors are modeled as white noises with an rms value on the order of 0.1 mrads.

The **positioning errors**, $v_{A_{PU}}$ and $v_{E_{PU}}$, are due to sources such as phase quantization and phase shifter errors. They are modeled as white noises with an rms on the order of 0.35 mrads.

Cross coupling between the sum and difference channel of the monopulse radar can result in a pointing error of the monopulse beam. The errors $v_{A_{CC}}$ and $v_{E_{CC}}$, resulting from channel cross coupling are modeled as white noises with an rms value on the order of 0.15 mrads.

Non-uniform gains across the face of the antenna array can also result in radar beam pointing errors. These errors are often referred to as "monopulse slope" errors. The **monopulse slope errors**, denoted $v_{A_{MS}}$ and $v_{E_{MS}}$, are modeled as white noises with an rms value on the order of 0.1 mrads.

In [11], **thermal noise** is modeled as white noise process. Therefore, the thermal noise errors, denoted $v_{A_{TN}}$ and $v_{E_{TN}}$, are modeled here as white noises with an rms value of 0.2 mrads.

Quantization errors will enter into the azimuth and elevation angle measurements as a result of the finite word length used in the digital computers which process the monopulse radar measurements. As mentioned earlier, quantization errors are often modeled as white noise processes. Consequently, the azimuth and elevation angle quantization errors, denoted v_{A_Q} and v_{E_Q}, are modeled as white noises with an rms value of the order of 0.2 mrads. The true rms value for this error is highly dependent on the design.

27

The antenna random will often bend the boresight of the radar. This bending is usually compensated by the radar processor; however, often there exists some uncompensated bending. The **uncompensated random bending errors**, denoted $v_{A_{RAD}}$ and $v_{E_{RAD}}$, are modeled as white noises with an rms value on the order of 0.4 mrads.

7.0 INS Indicated Range and Range Rate

The INS indicated measurements of range r and range rate $\dot{r}$ may be expressed by the following relationships:

$$\bar{r} = \sqrt{(\bar{p}^n)^T \bar{p}^n} \tag{86}$$

$$\bar{\dot{r}} = -(\bar{u}_p^n)^T \bar{v}_a^n \tag{87}$$

where $\bar{p}^n$ and $\bar{u}_p^n$ are computed form the INS indicated aircraft position $\bar{r}_a^n$ and the indicated target position $\bar{r}_t^n$.

$$\bar{p}^n = \bar{r}_t^n - \bar{r}_a^n \tag{88}$$

$$\bar{u}_p^n = \frac{\bar{p}^n}{\sqrt{(\bar{p}^n)^T \bar{p}^n}} \tag{89}$$

Notice that an indicated target position, denoted $\bar{r}_t^n$, is needed to compute the INS indicated measurement of range

and range rate. However, in general, it is not provided by the INS. The indicated target position, $\bar{r}_t^n$, may be obtained using a pre-briefed target position. If the pre-briefed target information is not available, simply compute the indicated target position from the first set of radar measurements.

INS indicated Azimuth and Elevation Angle Measurements

The indicated values of the unit vectors u_{py}^a and u_{pz}^a are obtained directly form Equations (22) and (23), i.e.

$$\bar{u}_{py}^a = [\ 0\ \ 1\ \ 0\ ]^T \tag{90}$$

$$\bar{u}_{pz}^a = [\ 0\ \ 0\ \ 1\ ]^T \tag{91}$$

Likewise, they may be converted to the navigation frame by employing coordinate transformations to obtain:

$$\bar{u}_{py}^n = \bar{C}_b^n \bar{C}_a^b \bar{u}_{py}^a = \bar{C}_a^n \bar{u}_{py}^a \tag{92}$$

$$\bar{u}_{pz}^n = \bar{C}_b^n \bar{C}_a^b \bar{u}_{pz}^a = \bar{C}_a^n \bar{u}_{pz}^a \tag{93}$$

The basic relationship between INS indicated measurements $\bar{A}$ and $\bar{E}$ and the unit vector of interest is

$$\cos(\bar{A}) = (\bar{u}_p^n)^T \bar{u}_{py}^n \tag{94}$$

$$\cos(\bar{E}) = (\bar{u}_p^n)^T \bar{u}_{pz}^n \tag{95}$$

Solving for $\bar{A}$ and $\bar{E}$ yields:

29

$$\bar{A} = \cos^{-1}\left[(\bar{\mathbf{u}}_p^n)^T\, \bar{\mathbf{u}}_{py}^n\right] \qquad (96)$$

$$\bar{E} = \cos^{-1}\left[(\bar{\mathbf{u}}_p^n)^T\, \bar{\mathbf{u}}_{pz}^n\right] \qquad (97)$$

8.0 Linearized INS Indicated Measurements

Derived in this section are the linearized equations for the INS indicated measurements. These equations will be used later to derive the Kalman filter measurement equations. Since coordinate transformations are required to compute INS indicated measurements, this section begins with a perturbation analysis of the INS indicated transformation matrices.

8.1 Transformation Matrix Perturbations

The indicated transformation matrices can be expressed as the sum of the true transformation matrix and the INS indicated transformation matrix error, i.e.

$$\bar{C}_b^n = C_b^n + \delta C_b^n \tag{98}$$

$$\bar{C}_a^b = C_a^b + \delta C_a^b \tag{99}$$

Next, we find an expression for the INS indicated body to navigation frame transformation matrix error δC_b^n. A similar development applies for the antenna to body frame transformation error δC_a^b. Since it is not needed for the analysis of relative SAR targeting, we do not consider the perturbations of the Earth to navigation frame transformation, heading to navigation frame transformation, and path to heading frame transformation.

The errors in the INS indicated body to navigation frame transformation matrix are a result of errors in the INS indicated Euler angles $(\bar{\alpha}_x, \bar{\alpha}_y, \bar{\alpha}_z)$ where,

$$\bar{\alpha}_x = \alpha_x + \delta\alpha_x \tag{100}$$

$$\bar{\alpha}_y = \alpha_y + \delta\alpha_y \tag{101}$$

$$\bar{\alpha}_z = \alpha_z + \delta\alpha_z \tag{102}$$

Substituting the INS indicated Euler angles in Equations (100), (101), and (102) for the true Euler angles in Equation (12) yields the following expression for the INS indicated transformation matrix.

$$\bar{C}_b^n = \begin{bmatrix} C(\bar{\alpha}_z)C(\bar{\alpha}_y) & C(\bar{\alpha}_z)S(\bar{\alpha}_y)S(\bar{\alpha}_x) - S(\bar{\alpha}_z)C(\bar{\alpha}_x) & C(\bar{\alpha}_z)S(\alpha_y)C(\bar{\alpha}_x) + S(\bar{\alpha}_z)S(\bar{\alpha}_x) \\ S(\bar{\alpha}_z)C\bar{\alpha}_y & S(\bar{\alpha}_z)S(\bar{\alpha}_y)S(\bar{\alpha}_x) + C(\bar{\alpha}_z)C(\bar{\alpha}_x) & S(\alpha_z)S(\bar{\alpha}_y)C(\bar{\alpha}_x) - C(\bar{\alpha}_z)S(\bar{\alpha}_x) \\ -S\alpha_y & C\alpha_y S(\bar{\alpha}_x) & C\alpha_y C(\bar{\alpha}_x) \end{bmatrix} \tag{103}$$

31

For "small" error angles (less than 5 degrees), the following approximations exits for the sin and cosine of an angle plus its error.

$$\sin(\theta + \delta\theta) \approx \sin(\theta) + \delta\theta \cos(\delta\theta) \tag{104}$$

$$\cos(\theta + \delta\theta) \approx \cos(\theta) - \delta\theta \sin(\theta) \tag{105}$$

Using equations (104) and (105) in Equation (103), expanding terms, and neglecting and 2nd and 3rd order error terms, we obtain the following expression for the INS indicated transformation matrix error.

$$\delta C_b^n \approx \begin{bmatrix} -\delta\alpha_z S\alpha_z C\alpha_y - \delta\alpha_y C\alpha_z S\alpha_y & -\delta\alpha_z S\alpha_z S\alpha_y S\alpha_x + \delta\alpha_y C\alpha_z C\alpha_y S\alpha_x + \delta\alpha_x C\alpha_z S\alpha_y C\alpha_x - \delta\alpha_z C\alpha_z C\alpha_x + \delta\alpha_x S\alpha_z S\alpha_x & \ldots \\ +\delta\alpha_z C\alpha_z C\alpha_y - \delta\alpha_y S\alpha_z S\alpha_y & +\delta\alpha_z C\alpha_z S\alpha_y S\alpha_x + \delta\alpha_y S\alpha_z C\alpha_y S\alpha_x + \delta\alpha_x S\alpha_z S\alpha_y C\alpha_x - \delta\alpha_z S\alpha_z C\alpha_x - \delta\alpha_x C\alpha_z S\alpha_x & \ldots \\ -\delta\alpha_y C\alpha_y & -\delta\alpha_y S\alpha_y S\alpha_x + \delta\alpha_x C\alpha_y C\alpha_x & \ldots \end{bmatrix}$$

$$\begin{bmatrix} -\delta\alpha_z S\alpha_z S\alpha_y C\alpha_x + \delta\alpha_y C\alpha_z C\alpha_y C\alpha_x - \delta\alpha_x C\alpha_z S\alpha_y S\alpha_x + \delta\alpha_z C\alpha_z S\alpha_x C\alpha_x + \delta\alpha_x S\alpha_z C\alpha_x \\ +\delta\alpha_z C\alpha_z S\alpha_y C\alpha_x + \delta\alpha_y S\alpha_z C\alpha_y C\alpha_x - \delta\alpha_x S\alpha_z S\alpha_y S\alpha_x + \delta\alpha_z S\alpha_z S\alpha_x + \delta\alpha_x C\alpha_z C\alpha_x \\ -\delta\alpha_y S\alpha_y C\alpha_x - \delta\alpha_x C\alpha_y S\alpha_x \end{bmatrix} \tag{106}$$

Due to their manipulative properties it is very desirable to work with orthogonal matrices. However, notice that the expression for δC_b^n in Equation (106) is nonorthogonal. In Britting [12], it is shown that the "optimal" orthogonal approximation to $\bar{C}_b^n$ in the sense that the trace of $[(\bar{C}_b^n)_o - \bar{C}_b^n]^T [(\bar{C}_b^n)_o - \bar{C}_b^n]$ is minimized is given by:

$$(\bar{C}_b^n)_o = \frac{\bar{C}_b^n}{\sqrt{[(\bar{C}_b^n)^T \cdot \bar{C}_b^n]}} \tag{107}$$

Substituting Equations (98) into Equation (107) and expanding the square root term in series, the result is

$$(\bar{C}_b^n)_o = (I + 0.5[\delta C_b^n (C_b^n)^T - C_b^n(\delta C_b^n)^T]) \ C_b^n \tag{108}$$

where I is a 3x3 identity matrix. Since it involves the difference between a matrix and its transpose, the bracketed term on the right-hand side of Equation (108) is skew symmetric. Consequently, Equation (108) can be written as:

$$(\bar{C}_b^n)_o = \{ I - \Psi \} \ C_b^n \tag{109}$$

where

$$\Psi = \begin{bmatrix} 0 & -\psi_z & \psi_y \\ \psi_z & 0 & -\psi_x \\ -\psi_y & \psi_x & 0 \end{bmatrix} \tag{110}$$

The non-zero elements of Ψ are given by:

$$\psi_x = 0.5[c_{31}\delta c_{21} - c_{21}\delta c_{31} + c_{32}\delta c_{22} - c_{22}\delta c_{32} + c_{33}\delta c_{23} - c_{23}\delta c_{33}] \tag{111}$$

$$\psi_y = 0.5[c_{11}\delta c_{31} - c_{31}\delta c_{11} + c_{13}\delta c_{32} - c_{32}\delta c_{13} + c_{13}\delta c_{33} - c_{33}\delta c_{13}] \tag{112}$$

$$\psi_z = 0.5[c_{21}\delta c_{11} - c_{11}\delta c_{21} + c_{22}\delta c_{12} - c_{12}\delta c_{22} + c_{23}\delta c_{13} - c_{13}\delta c_{23}] \tag{113}$$

where c_{ij} and δc_{ij} are the elements of C_b^n and δC_b^n, respectively, such that i is the row number and j is the column.

Similar to the above development, the indicated antenna to navigation transformation matrix may be computer by the following equation:

$$(\bar{C}_a^b)_0 = \{ I - B \} C_a^b \tag{114}$$

where

$$B = \begin{bmatrix} 0 & -\beta_z & \beta_y \\ \beta_z & 0 & -\beta_x \\ -\beta_y & \beta_x & 0 \end{bmatrix} \tag{115}$$

For a Kalman filter design, it is sufficient to work directly with the error angles, ψ_x, ψ_y, ψ_z, β_x, β_y, and β_z. However, to keep in mind that INS systems often provides only the Euler angles. Therefore, it may be necessary to compute the Kalman filter's estimate of the Euler angels. Therefore, it may be necessary to compute the Kalman filter's estimate of the Euler angel errors from the Kalman filter's estimate of ψ_x, ψ_y, and ψ_z, to perform a correction to the INS indicated Euler angels. For example, this may be done for the body to navigation Euler angles by equating Equation (106) to ΨC_b^n and solving for $\delta\alpha_x$, $\delta\alpha_y$, and $\delta\alpha_z$, and in terms of ψ_x, ψ_y, and ψ_z.

8.2 Linearized INS Indicated Range and Range Rate Measurements

The INS indicated position, $\bar{r}_a^n$, and the indicated target position $\bar{r}_t^n$ can be express as a sum of the true values and the error values, i.e.

$$\bar{r}_t^n = r_t^n + \delta r_t^n \tag{116}$$

$$\bar{r}_a^n = r_a^n + \delta r_a^n \tag{117}$$

Substituting, Equations (116) and (117) into Equation (88) yields

$$\bar{p}^n = p^n + \delta p^n = r_t^n + \delta r_t^n - r_a^n + \delta r_a^n \tag{118}$$

where $\delta p^n = \delta r_t^n - \delta r_a^n$

33

Express the INS indicated range $\bar{r}$ measurement in terms of its errors by including the errors δr_t^n and δr_a^n in Equation (86) to obtain

$$\bar{r} = \sqrt{[p^n + \delta r_t^n - \delta r_a^n]^T \, [p^n + \delta r_t^n - \delta r_a^n]} \qquad (119)$$

Rearranging Equation (119) and dropping second order error terms yields

$$\bar{r} \approx \sqrt{[(p^n)^T \, p^n]} \sqrt{1 + \frac{2(\delta r_t^n - \delta r_a^n)^T \, p^n}{[(p^n)^T \, p^n]}} \qquad (120)$$

Using the approximation $(1 + x)^m \approx (1 + mx)$ for $|x| \ll 1$, and rearranging, Equation (120) reduces to:

$$\bar{r} \approx r + \frac{(p^n)^T \, [\delta r_t^n - \delta r_a^n]}{\sqrt{[(p^n)^T \, p^n]}} \qquad (121)$$

$$\bar{r} \approx r + (u_p^n)^T \, [\delta r_t^n - \delta r_a^n] \qquad (122)$$

The INS indicated unit line-of-sight vector, $\bar{u}_p^n$, can be expressed as the sum of the true value and its error, i.e.

$$\bar{u}_p^n = u_p^n + \delta u_p^n \qquad (123)$$

Derived next is a linearized equation for δu_p^n. Substitute Equation (118) into Equation (89) to obtain

$$\bar{u}_p^n = \frac{p^n + \delta p^n}{\sqrt{[(p^n)^T + (\delta p^n)^T] \, [p^n + \delta p^n]}} \qquad (124)$$

Rearranging Equation (124) and dropping second-order error terms yields

$$\bar{u}_p^n = \frac{(p^n + \delta p^n)}{\sqrt{[(p^n)^T p^n + 2(p^n)^T \delta p^n]}} = \frac{1}{r} \frac{(p^n + \delta p^n)}{\sqrt{[1 + \frac{2(p^n)^T \delta p^n}{(p^n)^T p^n}]}} \qquad (125)$$

Using the approximation $(1 + x)^m \approx (1 + mx)$ for $|x| \ll 1$, Equation (125) reduces to:

$$\bar{u}_p^n = \frac{1}{r}(p^n + \delta p^n)\left[1 - \frac{(p^n)^T \delta p^n}{(p^n)^T p^n}\right] \qquad (126)$$

Rearranging Equation (126) and dropping second order error terms we obtain:

$$\bar{u}_p^n = u_p^n + \frac{1}{r}[I - u_p^n (u_p^n)^T]\delta p^n$$

$$\bar{u}_p^n = u_p^n + \frac{1}{r}[I - u_p^n (u_p^n)^T](\delta r_t^n - \delta r_a^n)$$

$$\bar{u}_p^n = u_p^n + \delta u_p^n \qquad (127)$$

where

$$\delta u_p^n = \frac{1}{r}[I - u_p^n (u_p^n)^T](\delta r_t^n - \delta r_a^n). \qquad (128)$$

34

The INS indicated Earth referenced velocity $\bar{v}_a^n$, can be expressed as a sum of the true value and the error value, i.e.

$$\bar{v}_a^n = v_a^n + \delta v_a^n \tag{129}$$

Expressed $\bar{r}$ in terms of its errors by including the errors δu_p^n and the INS indicated velocity error, δv_a^n, in Equation (86) to obtain:

$$\bar{\dot{r}} = - [(u_p^n)^T + (\delta u_p^n)^T][v_a^n + \delta v_a^n] \tag{130}$$

Rearranging Equation (130) and dropping all second order error terms yields

$$\bar{\dot{r}} \approx \dot{r} - [(\delta u_p^n)^T v_a^n] - [(u_p^n)^T \delta v_a^n] \tag{131}$$

Substituting $(\delta u_p^n)^T$ from Equation (128), we obtain

$$\bar{\dot{r}} \approx \dot{r} - (v_a^n)^T \frac{1}{r} [I - u_p^n(u_p^n)^T][\delta r_t^n - \delta r_a^n] - (u_p^n)^T \delta v_a^n \tag{132}$$

Equation (132) can be written more compactly by defining

$$L \triangleq \frac{1}{r} [I - u_p^n(u_p^n)^T] \tag{133}$$

to obtain

$$\bar{\dot{r}} \approx \dot{r} + (v_a^n)^T L \delta r_t^n - (v_a^n)^T L \, \delta r_a^n - (u_p^n)^T \delta v_a^n \tag{134}$$

8.3 Linearized INS Indicated Azimuth and Elevation Angles Measurements

The INS indicated measurements of the azimuth angle $\bar{A}$ and the elevation angle $\bar{E}$ are expressed as the sum of the true value and the error.

$$\bar{A} = A + \delta A \tag{135}$$

$$\bar{E} = E + \delta E \tag{136}$$

The development that follows next is only for the azimuth measurement; but it also applies to the elevation measurement.

To get an expression describing δA, form the difference between $\cos(\bar{A})$ and $\cos(A)$ and call it $\Delta\cos$.

$$\Delta\cos = \cos(\bar{A}) - \cos(A) \tag{137}$$

$$\Delta\cos = \cos(A + \delta A) - \cos(A) \tag{138}$$

Using the approximation found in Equation (105), $\cos(\theta + \delta\theta) = \cos(\theta) - \delta\theta\sin(\theta)$ for "small" $\delta\theta$, Equation (137) reduces to:

$$\Delta \cos = -\delta A \sin(A) \tag{139}$$

Solving for δA yields,

$$\delta A = \frac{-\Delta \cos}{\sin(A)} \tag{140}$$

$$\delta A = \frac{[(\bar{\mathbf{u}}_p^n)^T \bar{\mathbf{u}}_{py}^n - (\mathbf{u}_p^n)^T \mathbf{u}_{py}^n]}{\sin(A)} \tag{141}$$

$$\delta A \approx \frac{(\mathbf{u}_p^n)^T \delta \mathbf{u}_{py}^n}{-\sin(A)} + \frac{(\mathbf{u}_p^n)^T \delta \mathbf{u}_{py}^n}{-\sin(A)} \tag{142}$$

At this point it becomes necessary to derive an expression for $\delta \mathbf{u}_{py}^n$. It may be found by subtracting $\mathbf{u}_{py}^n$ from $\bar{\mathbf{u}}_{py}^n$

and recognizing the fact that $\bar{\mathbf{u}}_{py}^b = \mathbf{u}_{py}^b$ to obtain the following

$$\delta \mathbf{u}_{py}^n = \bar{\mathbf{u}}_{py}^n - \mathbf{u}_{py}^n \tag{143}$$

$$\delta \mathbf{u}_{py}^n = (\bar{C}_b^n \bar{C}_a^b - \bar{C}_a^n) \, \mathbf{u}_{py}^n \tag{144}$$

$$\delta \mathbf{u}_{py}^n \approx (-\Psi - C_b^n \mathbf{B} C_n^b) \, \mathbf{u}_{py}^n \tag{145}$$

$$\delta \mathbf{u}_{py}^n \approx [-(\psi)^* - C_b^n (\beta)^* C_n^b] \, \mathbf{u}_{py}^n \tag{146}$$

$$\delta \mathbf{u}_{py}^n \approx -(\gamma)^* \, \mathbf{u}_{py}^n \tag{147}$$

$$\delta \mathbf{u}_{py}^n \approx \mathbf{u}_{py}^n \, \gamma^* \tag{148}$$

where the superscript $*$ denotes the skew-symmetric form of a vector and $\psi = [\psi_x, \psi_y, \psi_z]^T$, the vector

$\beta = [\beta_x, \beta_y, \beta_z]^T$, and $(\gamma)^* = (\psi)^* + C_b^n (\beta)^* C_n^b$. Substituting Equation (148) and (128) into Equation (142) yields

the expression

$$\delta A \approx \frac{(\mathbf{u}_p^n)^T (\mathbf{u}_{py}^n)^* \gamma + \frac{1}{r} (\mathbf{u}_{py}^n)^T [\, I - \mathbf{u}_p^n (\mathbf{u}_p^n)^T](\delta \mathbf{r}_t^n - \delta \mathbf{r}_a^n)}{-\sin(A)} \tag{149}$$

In [1], it is shown that the gradient of A in the navigation frame, denoted ∇A^n, is expressed by the following

$$(\nabla A^n)^T = \frac{(\mathbf{u}_{py}^n)^T [\, I - \mathbf{u}_p^n (\mathbf{u}_p^n)^T]}{-r \sin(A)}, \tag{150}$$

Using the result, Equation (149) can be written more compactly as

$$\delta A \approx \frac{(\mathbf{u}_p^n)^T (\mathbf{u}_{py}^n)^* \gamma}{-r \sin(A)} + (\nabla A^n)^T [\delta \mathbf{r}_t^n - \delta \mathbf{r}_a^n] \tag{151}$$

The first term in Equation (151) may also be expressed in terms of ∇A^n after the following manipulations:

$$\frac{(\mathbf{u}_p^n)^T(\mathbf{u}_{py}^n)*\gamma}{-\sin(A)} = \frac{-1}{\sin(A)}\mathbf{u}_p^n(\mathbf{u}_{py}^n \times \gamma) \tag{152}$$

$$\frac{(\mathbf{u}_p^n)^T(\mathbf{u}_{py}^n)*\gamma}{-\sin(A)} = \frac{-1}{\sin(A)}(\mathbf{u}_p^n \times \mathbf{u}_{py}^n) \cdot \gamma \tag{153}$$

$$\frac{(\mathbf{u}_p^n)^T(\mathbf{u}_{py}^n)*\gamma}{-\sin(A)} = \frac{-1}{\sin(A)}\{[\mathbf{u}_p^n \times (\mathbf{u}_p^n \times \mathbf{u}_{py}^n)] \times \mathbf{u}_p^n\} \cdot \gamma \tag{154}$$

$$\frac{(\mathbf{u}_p^n)^T(\mathbf{u}_{py}^n)*\gamma}{-\sin(A)} = \frac{-1}{\sin(A)}[\mathbf{u}_p^n \times (\mathbf{u}_p^n \times \mathbf{u}_{py}^n)] \cdot [\mathbf{u}_p^n \times \gamma] \tag{155}$$

$$\frac{(\mathbf{u}_p^n)^T(\mathbf{u}_{py}^n)*\gamma}{-\sin(A)} = \frac{-1}{\sin(A)}[(\mathbf{u}_p^n \cdot \mathbf{u}_{py}^n)\ \mathbf{u}_p^n - (\mathbf{u}_p^n \cdot \mathbf{u}_p^n)\ \mathbf{u}_{py}^n] \cdot [\mathbf{u}_p^n \times \gamma] \tag{156}$$

$$\frac{(\mathbf{u}_p^n)^T(\mathbf{u}_{py}^n)*\gamma}{-\sin(A)} = \frac{1}{\sin(A)}[\mathbf{u}_{py}^n - (\mathbf{u}_{py}^n \cdot \mathbf{u}_p^n)\ \mathbf{u}_p^n] \cdot [\mathbf{u}_p^n \times \gamma] \tag{157}$$

$$\frac{(\mathbf{u}_p^n)^T(\mathbf{u}_{py}^n)*\gamma}{-\sin(A)} = \frac{(\mathbf{u}_{py}^n)^T}{\sin(A)}[\ I - \mathbf{u}_p^n(\mathbf{u}_p^n)^T](\mathbf{u}_p^n)*\gamma \tag{158}$$

$$\frac{(\mathbf{u}_p^n)^T(\mathbf{u}_{py}^n)*\gamma}{-\sin(A)} = -r(\nabla A^n)^T(\mathbf{u}_p^n)*\gamma \tag{159}$$

$$\frac{(\mathbf{u}_p^n)^T(\mathbf{u}_{py}^n)*\gamma}{-\sin(A)} = -r(\nabla A^n)^T(\mathbf{u}_p^n)*\psi - r(\nabla A^n)^T(\mathbf{u}_p^n)*C_b^n\beta \tag{160}$$

where $\cdot$ and $\times$ denote the inner and cross products, respectively. Equations (154) and (156) were obtained by direct application of the vector triple product expansion. Substituting the result of Equation (160) into Equation (151) yields

$$\delta A \approx -r(\nabla A^n)^T(\mathbf{u}_p^n)*\psi - r(\nabla A^n)^T(\mathbf{u}_p^n)*C_b^n\beta + (\nabla A^n)^T \delta\mathbf{r}_t^n - (\nabla A^n)^T \delta\mathbf{r}_a^n \tag{161}$$

By a method similar to that described above for the azimuth measurement, the corresponding equations for the elevation measurements are given by:

$$\delta E \approx -r(\nabla E^n)^T(\mathbf{u}_p^n)*\psi - r(\nabla E^n)^T(\mathbf{u}_p^n)*C_n^b\beta + (\nabla E^n)^T \delta\mathbf{r}_t^n - (\nabla E^n)^T \delta\mathbf{r}_a^n \tag{162}$$

where

$$(\nabla E^n)^T = \frac{(\mathbf{u}_{pz}^n)^T}{r\sin(E)}[\ I - \mathbf{u}_p^n(\mathbf{u}_p^n)^T]$$

$$\tag{163}$$

Thus, the linearized INS indicated measurements of the azimuth and elevation angles are given by:

37

$$\bar{A} \approx A - r(\nabla A^n)^T (\mathbf{u}_p^n)^* \psi - r(\nabla A^n)^T (\mathbf{u}_p^n)^* C_b^n \beta + (\nabla A^n)^T \delta \mathbf{r}_t^n - (\nabla A^n)^T \delta \mathbf{r}_a^n \tag{164}$$

$$\bar{E} \approx E - r(\nabla E^n)^T (\mathbf{u}_p^n)^* \psi - r(\nabla E^n)^T (\mathbf{u}_p^n)^* C_b^n \beta + (\nabla E^n)^T \delta \mathbf{r}_t^n - (\nabla E^n)^T \delta \mathbf{r}_a^n \tag{165}$$

respectively.

9.0 Kalman Filter Measurements

This section derives the equations for the Kalman filter measurements. Also, derived here are the linearized measurement equations needed for designing a Kalman filter.

The inputs to the Kalman filter are the difference between the INS indicated measurements and the radar measured values, i.e.,

$$z_r = \bar{r} - \tilde{r} \tag{166}$$

$$z_{\dot{r}} = \bar{\dot{r}} - \tilde{\dot{r}} \tag{167}$$

$$z_A = \bar{A} - \tilde{A} \tag{168}$$

$$z_E = \bar{E} - \tilde{E} \tag{169}$$

In a Kalman filter design, it is necessary to linearize any non-linear measurement equations. The linearized Kalman filter measurement may be obtained by differencing the linearized indicated measurements and the radar measurements to obtain:

$$z_r = (u_p^n)^T [\delta r_t^n - \delta r_a^n] - \delta r_{CL} - r\delta C + v_{r_{DES}} + v_{r_Q} + v_{r_T} + v_{r_{OT}} \tag{170}$$

$$z_{\dot{r}} = (v_a^n)^T L \delta r_t^n - (v_a^n)^T L \delta r_a^n - (u_p^n)^T [\delta v_a^n] - \delta \dot{r}_D - \dot{r}\delta C - \dot{r}\delta F + v_{\dot{r}_{DES}} + v_{\dot{r}_Q} + v_{\dot{r}_T} + v_{\dot{r}_{OT}} \tag{171}$$

$$z_A = -r(\nabla A^n)^T (u_p^n)^* \psi - r(\nabla A^n)^T (u_p^n)^* C_b^n \beta + (\nabla A^n)^T \delta r_t^n - (\nabla A^n)^T \delta r_a^n - \delta A_{TEMP}$$

$$+ v_{A_{MA}} + v_{A_{FL}} + v_{A_{PU}} + v_{A_{CC}} + v_{A_{MS}} + v_{A_{TN}} + v_{A_Q} + v_{A_{RAD}} \tag{172}$$

$$z_E = -r(\nabla E^n)^T (u_p^n)^* \psi - r(\nabla E^n)^T (u_p^n)^* C_b^n \beta + (\nabla E^n)^T \delta r_t^n - (\nabla E^n)^T \delta r_a^n - \delta E_{TEMP}$$

$$+ v_{E_{MA}} + v_{E_{FL}} + v_{E_{PU}} + v_{E_{CC}} + v_{E_{MS}} + v_{E_{TN}} + v_{E_Q} + v_{E_{RAD}} \tag{173}$$

10.0 Error State Differential Equations

The error state differential equations for an INS have been presented in [4, 13, 14, 15]. The result of this work as well as the results presented in this report concerning radar error states are presented in this section.

The basic definition for the error state vectors associated with the INS indicated outputs and the SAR and monopulse radar measurements are given as:

$$x_{\text{Ind}} = [(\delta r_a^n)^T ((\delta v_a^n)^T \psi^T \nabla^T k_\nabla^T \varepsilon^T k_\varepsilon^T (\delta r_t^n)^T \beta^T]^T \tag{174}$$

$$x_{\text{Radar}} = [\delta r_{\text{CL}} \; \delta \dot{r}_D \; \delta C \; \delta F \; \delta A_{\text{TEMP}} \; \delta E_{\text{TEMP}}]^T \tag{175}$$

where ∇ is the accelerometer bias vector, k_∇ is the accelerometer scale factor bias vector, ε is the gyro bias vector, and k_ε is the gyro scale factor bias vector.

Generally, the error states are modeled as linear differential equations of the form:

$$\dot{x}(t) = F(t)x(t) + w(t) \tag{176}$$

Consider the augmented state vector $x = [x_{\text{Ind}}^T \; x_{\text{Radar}}^T]^T$ considering of both the indicated output error states and radar error states. Using this augmented vector, Equation (176) may be written as:

$$\begin{bmatrix} \dot{x}_{\text{Ind}} \\ \dot{x}_{\text{Radar}} \end{bmatrix} = \begin{bmatrix} F_{\text{Ind}}(t) & 0 \\ 0 & F_{\text{Radar}}(t) \end{bmatrix} \begin{bmatrix} x_{\text{Ind}} \\ x_{\text{Radar}} \end{bmatrix} + \begin{bmatrix} w_{\text{Ind}} \\ w_{\text{Radar}} \end{bmatrix} \tag{177}$$

The fundamental dynamic matrix F_{Ind}, is given in Table 1.

Table 1. Indicated output error state dynamic matrix F_{Ind}.

	δr_a^n	δv_a^n	ψ	∇	k_∇	ε	k_ε	δr_t^e	β
$\dot{\delta r}_a^n$	0	I	0	0	0	0	0	0	0
$\dot{\delta v}_a^n$	F_{vr}	F_{vv}	$F_{v\psi}$	I	A^d	0	0	0	0
$\dot{\psi}$	0	0	$-\omega^*$	0	0	I	ω^d	0	0
$\dot{k}_\nabla$	0	0	0	0	0	0	0	0	0
$\dot{\nabla}$	0	0	0	0	0	0	0	0	0
$\dot{\varepsilon}$	0	0	0	0	0	0	0	0	0
$\dot{k}_\varepsilon$	0	0	0	0	0	0	0	0	0
$\dot{\delta r}_t^e$	0	0	0	0	0	0	0	0	0
β	0	0	0	0	0	0	0	0	0

40

where,

$$\mathbf{F}_{vr} = \begin{bmatrix} \omega^2 - \omega_s^2 - \Omega^2 - (\omega_x + \Omega_x)\rho_x & \dot{\rho}_x - [\omega_y + \Omega_y]\,\rho_x & -\dot{\rho}_y - [\omega_z + \Omega_z]\,\rho_x \\ -\dot{\rho}_z - [\omega_x + \Omega_x]\,\rho_y & \omega^2 - \omega_s^2 - \Omega^2 - (\omega_y + \Omega_y)\rho_x & \dot{\rho}_x - [\omega_z + \Omega_z]\,\rho_y \\ \dot{\rho}_y - [\omega_x + \Omega_x]\,\rho_z & -\dot{\rho}_z - [\omega_y + \Omega_y]\,\rho_z & \omega^2 - \omega_s^2 - \Omega^2 - (\omega_x + \Omega_z)\rho_z \end{bmatrix} \tag{178}$$

$$\mathbf{F}_{vv} = \begin{bmatrix} 0 & 2\omega_z & -2\omega_y \\ -2\omega_z & 0 & 2\omega_x \\ 2\omega_y & -2\omega_x & 0 \end{bmatrix} \tag{179}$$

$$\mathbf{F}_{v\psi} = \begin{bmatrix} 0 & A_z & -A_y \\ -A_z & 0 & A_x \\ A_y & -A_x & 0 \end{bmatrix} \tag{180}$$

$$\omega^* = \begin{bmatrix} 0 & -\omega_z & \omega_y \\ \omega_z & 0 & -\omega_x \\ -\omega_y & \omega_x & 0 \end{bmatrix} \tag{181}$$

where $\mathbf{A}$ is the acceleration, ρ is the angular rate from the Earth fixed coordinates to the navigation coordinates, Ω is the Earth's angular rate relative to inertial coordinates, ω is the angular rate from inertial to platform coordinates ($\omega = \Omega + \rho$), $\omega_s^2 = g/R$ is the Schuler frequency squared, g is the gravitational acceleration, R is the Earth's radius, $\omega^2 = \omega^T\omega$. The subscripts x, y, and z correspond to the directions in the navigation frame. Finally, the d superscript on a vector is used to denote a diagonal matrix where the diagonal elements consists of elements of the vector, e.g.

$$\mathbf{A}^d = \begin{bmatrix} A_x & 0 & 0 \\ 0 & A_y & 0 \\ 0 & 0 & A_z \end{bmatrix} \tag{182}$$

The matrix $\mathbf{F}_{Radar}$ for the radar errors is given in Table 2. The vectors used to form the noise vector $\mathbf{w}$ are defined below:

41

Table 2. Radar error state dynamic matrix F_{Radar}.

	δr_{CL}	$\delta \dot{r}_D$	δC	δF	δA_{TEMP}	δE_{TEMP}
$\dot{\delta r}_{CL}$	0	0	0	0	0	0
$\dot{\delta \dot{r}}_{D}$	0	0	0	0	0	0
$\dot{\delta C}$	0	0	0	0	0	0
$\dot{\delta F}$	0	0	0	0	0	0
$\dot{\delta A}_{TEMP}$	0	0	0	0	$-\beta_{A_{TEMP}}$	0
$\dot{\delta E}_{TEMP}$	0	0	0	0	0	$-\beta_{E_{TEMP}}$

$$\mathbf{w}_{Ind} = [0^T \ \mathbf{w}_v^T \ \mathbf{w}_\psi^T \ 0^T \ 0^T \ 0^T \ 0^T \ 0^T]^T \tag{183}$$

$$\mathbf{w}_{Radar} = [0 \ 0 \ 0 \ 0 \ \omega_{A_{TEMP}} \ \omega_{E_{TEMP}}]^T \tag{184}$$

where $\mathbf{w}_v$ is the accelerometer white noise vector, $\mathbf{w}_\psi$ is the gyro white noise vector.

11.0 Linearized Measurement Model Summary

In general, a linearized measurement model is given by equations of the form:

$$\mathbf{z} = H\,\mathbf{x} + \mathbf{v}. \tag{185}$$

where H is the measurement matrix and $\mathbf{v}$ is the measurement white noise. This section summarizes the linearized measurement model derived in this report by expressing the results in the form of Equation (185).

$$\mathbf{z} = \begin{bmatrix} H_{Ind} & H_{Radar} \end{bmatrix} \begin{bmatrix} x_{Ind} \\ x_{Radar} \end{bmatrix} + \mathbf{v} \tag{186}$$

Tables 3 and 4 provide a summary of the error measurement matrices H_{Ind} and H_{Radar}. The measurement white noise vector $\mathbf{v}$ is given by:

$$\mathbf{v} = \begin{bmatrix} v_{r_{DES}} + v_{r_Q} + v_{r_T} + v_{r_{OT}} \\ v_{\dot{r}_{DES}} + v_{\dot{r}_Q} + v_{\dot{r}_T} + v_{\dot{r}_{OT}} \\ v_{A_{MA}} + v_{A_{FL}} + v_{A_{PU}} + v_{A_{CC}} + v_{A_{MS}} + v_{A_{TN}} + v_{A_Q} + v_{A_{RAD}} \\ v_{E_{MA}} + v_{E_{FL}} + v_{E_{PU}} + v_{E_{CC}} + v_{E_{MS}} + v_{E_{TN}} + v_{E_Q} + v_{E_{RAD}} \end{bmatrix} \tag{187}$$

Table 3. Error Measurement matrix (H_{Ind}).

	$\delta \mathbf{r}_a^n$	$\delta \mathbf{v}_a^n$	ψ	∇	k_∇	ε	k_ε	$\delta \mathbf{r}_t^e$	β
z_r	$-(\mathbf{u}_p^n)^T$	0	0	0	0	0	0	$(\mathbf{u}_p^n)^T C_e^n$	0
$z_{\dot{r}}$	$-(\mathbf{v}_a^n)^T L$	$-(\mathbf{u}_p^n)^T$	0	0	0	0	0	$(\mathbf{v}_a^n)^T L C_e^n$	0
z_A	$-(\nabla A^n)^T$	0	$-r(\nabla A^n)^T (\mathbf{u}_p^n)*$	0	0	0	0	$(\nabla A^n)^T C_e^n$	$-r(\nabla A^n)^T (\mathbf{u}_p^n)* \; C_b^n$
z_E	$-(\nabla E^n)^T$	0	$-r(\nabla E^n)^T (\mathbf{u}_p^n)*$	0	0	0	0	$(\nabla E^n)^T C_e^n$	$-r(\nabla E^n)^T (\mathbf{u}_p^n)* \; C_b^n$

$$L \triangleq -\frac{1}{r}[I - \mathbf{u}_p^n(\mathbf{u}_p^n)^T] \; ; \quad (\nabla A^n)^T = \frac{-(\mathbf{u}_{py}^n)^T}{r\sin(A)}[I - \mathbf{u}_p^n(\mathbf{u}_p^n)^T] \; ; \quad (\nabla E^n)^T = \frac{-(\mathbf{u}_{pz}^n)^T}{r\sin(E)}[I - \mathbf{u}_p^n(\mathbf{u}_p^n)^T]$$

Table 4. Error measurement matrix H_{Ind}.

	$\delta \mathbf{r}_{CL}$	$\delta \dot{\mathbf{r}}_D$	δC	δF	δA_{TEMP}	δE_{TEMP}
z_r	-1	0	-r	0	0	0
$z_{\dot{r}}$	0	-1	$-\dot{r}$	$-\dot{r}$	0	0
z_A	0	0	0	0	-1	0
z_E	0	0	0	0	0	-1

43

12.0 Summary of Errors Budget

Table 5 contains a proposed error budget for an INS and SAR system. This table was compiled from data available in [16] for the Honeywell H423 strapdown inertial navigation system. Tables 6 and 7 contain a summary of the error budget, described in this report, for SAR and monopulse radar measurements, respectively. These tables were compiled partially from a composition of data from the available literature and partially from experience and engineering intuition.

Table 5. INS Error Budget Summary.

Error	Error Description	RMS Value	Correlation Time
∇	Acceleration Bias	30 μg	bias
k_∇	Accelerometer Scale Factor Bias	175 PPM	bias
w_v	Accelerometer White Noise	0.0025 FPS $\sqrt{Hz}$	white
ε	Gyro Bias	0.004 Deg /Hr	bias
k_ε	Gyro Scale Factor Bias	2 PPM	bias
w_ψ	Gyro White Noise	0.0020Deg/Hr/$\sqrt{Hz}$	white

Table 6. SAR Geometry Error Budget Summary.

Error	Error Description	RMS Value	Correlation Time
δr_{CL}	Range Clock Error	0.01 feet	bias
$\delta \dot{r}_D$	Doppler Measurement Error	0.001 feet/sec	bias
δC	Propagation Speed Error	10 PPM	bias
δF	Frequency Error	20 PPM	bias
$v_{r_{DES}}$	Range Designation Error	2 Δr	white
$v_{\dot{r}_{DES}}$	Range Rate Designation Error	2 $\Delta \dot{r}$	white
v_{r_Q}	Range Quantization Error	$\Delta r / \sqrt{12}$	white
$v_{\dot{r}_Q}$	Range Rate Quantization Error	$\Delta \dot{r} / \sqrt{12}$	white
v_{r_T}	Range Timing Error	$T_d \dot{r}$	white
$v_{\dot{r}_T}$	Range Rate Timing Error	$T_d \ddot{r}$	white
$v_{r_{OT}}$	Range Miscellaneous	0.5 Δr	white
$v_{\dot{r}_{OT}}$	Range Rate Miscellaneous Errors	0.5 $\Delta \dot{r}$	white

44

Table 7. Monopulse Radar Error Budget Summary.

Error	Error Description	RMS Value	Correlation Time
β	Antenna Roll, Pitch, and Yaw Errors	1.20 *mrad*	bias
δA_{TEMP}	Azimuth Temperature Induced Errors	0.40 *mrad*	bias
δE_{TEMP}	Elevation Temperature Induced Errors	0.40 *mrad*	bias
$v_{A_{MA}}$	Azimuth Mechanical Alignment Error	0.30 *mrad*	white
$v_{E_{MA}}$	Elevation Mechanical Alignment Error	0.30 *mrad*	white
$v_{A_{FL}}$	Azimuth Flexure Error	0.10 *mrad*	white
$v_{E_{FL}}$	Elevation Flexure Error	0.10 *mrad*	white
$v_{A_{PU}}$	Azimuth Radome Phase Uniformity Error	0.35 *mrad*	white
$v_{E_{PU}}$	Elevation Radome Phase Uniformity Error	0.35 *mrad*	white
$v_{A_{CC}}$	Azimuth Rx Channel Cross Coupling Error	0.15 *mrad*	white
$v_{E_{CC}}$	Elevation Rx Channel Cross Coupling Error	0.15 *mrad*	white
$v_{A_{MS}}$	Azimuth Monopulse Slope Error	0.10 *mrad*	white
$v_{E_{MS}}$	Elevation Monopulse Slope Error	0.10 *mrad*	white
$v_{A_{TN}}$	Azimuth Thermal Noise	0.20 *mrad*	white
$v_{E_{TN}}$	Elevation Thermal Noise	0.20 *mrad*	white
v_{A_Q}	Azimuth Quantization Error	0.20 *mrad*	white
v_{E_Q}	Elevation Quantization Error	0.20 *mrad*	white
$v_{A_{RAD}}$	Azimuth Radome Error	0.40 *mrad*	white
$v_{E_{RAD}}$	Elevation Radome Error	0.40 *mrad*	white

45

13.0 Conclusions

The main objectives of this report were to provide some basic background on SAR targeting, describe the SAR measurements and measurement errors, and present a derivation of the equations needed to integrate navigation and SAR measurements in a Kalman filter. The focus of this report is on the integration of SAR with an inertial navigation system.

In this report, we have presented an introduction to "unfocused line-by-line" processed SAR, "focused line-by-line" processed SAR, and Doppler processed SAR. We have explained how each SAR measurement is obtained and how various error sources affect the measurements. Both the SAR measurement errors and inertial navigation errors were characterized by Stochastic models. Finally, we have derived both the non-linear and linear measurement equation used in a Kalman filter.

The proposed Kalman Filter design provides an optimal means to integrate SAR and INS data. It is capable of utilizing the entire history of SAR measurements over multiple SAR images to improve both SAR and INS measurements.

The location of the desired targets may or may not be known *a priori*. If the target's location is known *a priori* via intelligence information, then the Kalman filter's estimate is initialized with this data. Subsequent SAR measurement are then used to improve and refine the *a priori* intelligence data. When the target's location is not known *a priori*, the Kalman filter is initialized with the location computed from the first set of SAR measurements. This method is useful when the mission requires locating "targets of opportunity".

14.0 References

[1] Musick, S. H., "Radar measurements and measurement matrices," Tech Rep. AFAL-TM-76-48, Wright Laboratory (AFMC), Wright Patterson AFB, Ohio, May 1976.

[2] Jeffers, R. H. , A. B. Biererman, R. H. Rosen, B. S. Freeman, L. R. Doan, A. Mendelovicz, and B. L. Schutle, "SAR targeting accuracy analysis program (STAAP) - Hughes Aircraft Company, final report," Tech Rep. AFWAL-TR-88-1024, Wright Laboratory (AFMC), Wright Patterson AFB, Ohio, October 1988.

[3] Grettenberg, T. L., H. F. Lynn, and J. F. Bernuy, "SAR targeting accuracy analysis program (STAAP) - Emerson Electric Company, final report," Tech Rep. AFWAL-TR-88-1030, Wright Laboratory (AFMC), Wright Patterson AFB, Ohio, June 1988.

[4] Maybeck, P., *Stochastic Models, Estimation and Control, Volume 1*. San Diego, CA, Academic Press, Inc., 1979.

[5] Scmidt, D. J., "Error analysis of an air-to-surface missile with a synthetic aperture radar seeker," NAECON, pp. 363-370, Dayton, OH, May 1981.

[6] Nelander, J. C., A. C. Kenton, and J. A. Wright, "Performance sensitivities of position and velocity determination using SAR vision guidance updates," Proceedings of the Southeastern Conference on Energy and Information Technologies in the Southeast, pp. 90-94, Columbia, SC, April 1989.

[7] Kenton, A. C., J. A. Wright, and J. C. Nelander, "Vision guidance update: synthetic aperture radar (SAR) multiple image exploitation for position and velocity determination," SPIE Millimeter Wave and Synthetic Aperture Radar, vol. 1101, pp. 158-169, 1989.

[8] Heller, W. G, "Models for aided inertial navigation system sensor errors," Tech. Rep. TR-312-3, The Analytic Sciences Corporation, Reading, MA, Feb 1975.

[9] Meer, D. E., "Synthetic aperture radar." Air Force Institute of Technology, WPAFB, OH, Course Notes.

[10] Lathi, B. P., *Modern Digital and Analog Communication Systems*. Fort Worth, TX; Holt, Rinehart, and Winston, Inc., 1989.

[11] Peebles, P. Z. ed *Probability, Random Variables, and Random Signal Principles*. New York, NY; McGraw-Hill Book Company, 1987.

[12] Britting, K. R., *Inertial Navigation System Analysis*. New York, NY: Wiley-Interscience, 1971.

[13] Pinson, J. C., "Inertial guidance for cruise vehicles," in Guidance and Control of Aerospace Vehicles (C. T. Leondes, ed), New York, NY: McGraw Hill, 1963.

[14] Pitman, G.R.ed., *Inertial Guidance*. New York, NY: Wiley, 1962.

[15] Widnall, W. S. and P. A. Grundy, "Inertial navigation system error models," Tech Rep. Intermetrics TR-03-73, Intermetrics, Inc. Cambridge, MA, May 1973.

[16] Military Avionics Division, "Honeywell H423 performance accuracy (truth model-error budget) analysis," Tech. Rep. 1184-10121, Honeywell, Clearwater, FL, November 1984.